Vortex Properties of the High-Temperature Superconductor $Bi_2Sr_2CaCu_2O_{8+\delta}$, and Controlled Deposition of Carbon Nanotubes

by

Yan Mei Aileen Wang

B.A. (University of California at Los Angeles) 1996

A dissertation submitted in partial satisfaction of the
requirements for the degree of
Doctor of Philosophy

in

Physics

in the

GRADUATE DIVISION
of the
UNIVERSITY of CALIFORNIA at BERKELEY

Committee in charge:

Professor Alex Zettl, Chair
Professor Marvin Cohen
Professor Norman Phillips

Fall 2002

Vortex Properties of the High-Temperature Superconductor

$Bi_2Sr_2CaCu_2O_{8+\delta}$, and Controlled Deposition of Carbon Nanotubes

Abstract

Vortex Properties of the High-Temperature Superconductor $Bi_2Sr_2CaCu_2O_{8+\delta}$, and

Controlled Deposition of Carbon Nanotubes

by

Yan Mei Aileen Wang

Doctor of Philosophy in Physics
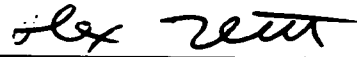
University of California at Berkeley

Professor Alex Zettl, Chair

This thesis contains two sections. The first section discusses vortex matter behavior in a high temperature superconductor, $Bi_2Sr_2CaCu_2O_{8+\delta}$ (BSCCO), studied using transport and local magnetization measurements. Vortex matter phase transitions in micron-sized BSCCO are investigated using GaAs/AlGaAs Hall sensors. We observe that the vortex solid 3D-2D phase transition disappears below a temperature-dependent critical sample size. Vortex penetration field measurements in micron-sized BSCCO show that the Bean-Livingston surface barrier effect dictates the vortex penetration field at high temperatures, and the bulk pinning effect dictates the vortex penetration field at low temperatures. When measuring the c-axis magneto-resistance of BSCCO in tilted magnetic fields, we observe that the in-plane pancake vortices arrange in a zigzag structure along the c-axis of the sample at low tilt angles and high magnetic fields. This zigzag arrangement lowers the

interaction energy of pancakes with Josephson vortices. Finally, in order to avoid the Bean-Livingston surface barrier effect, we measured vortex dissipation in BSCCO using a Corbino disk contact geometry. We found that, the vortex matter transport properties in BSCCO are determined by sample bulk properties, and not the Bean-Livingston surface barrier effect.

The second section of this thesis discusses the controlled deposition and manipulation of single carbon nanotubes using MEMS (Microelectromechanical systems) devices. Large-scale controlled deposition of individual nanotubes is a crucial requirement for realistic applications of nanotube-based electronic devices. Using novel substrate designs, we deposit single aligned nanotubes with complete control utilizing capillary forces and dielectrophoresis. We can also pull and bend the deposited single nanotubes *in situ* in a Transmission Electron Microscope.

The majority of the measurements on BSCCO and carbon nanotubes discussed here are made possible by the development of novel micro-fabrication techniques using the Micro-fabrication Laboratory facilities at UC Berkeley.

Professor Alex Zettl
Dissertation Committee Chair

Contents

List of Figures

.

Acknowledgements

There are many people I want to thank.

First, I would like to thank my advisor, Alex Zettl, for his guidance throughout the past five years. His hands-off style allowed me to pursue research projects that I believed to be interesting and "revolutionary". I want to thank him especially for his support during my toughest time at Cal - when I was struggling with the preliminary exam.

I want to thank Prof. Tamegai at University of Tokyo, for his help in all aspects of my high T_c superconductivity research. Although I first worked with him as a collaborator, yet he has been more like a mentor and a friend to me.

My interaction with Michael Fuhrer (now a professor at University of Maryland) started from my first day in lab. He taught me most of the transport measurement skills for studying high T_c materials and has always been very helpful. As a starting student, I was fortunate to have learned from him.

I enjoyed my years in lab together with all group members, previous and present ones. I thank Jian Ma for showing me the opportunities in industry, Phil Collins for helping me out on programming the stepper motor, and Kasra Khazeni and James Hone for showing me how to solder (hard and soft soldering). While Keith Bradley's easy-going personality makes my weekdays in lab pleasant, John Cumings' parties are the fun for the weekends. Current group members, which include Masa Ishigami, William Mickelson, Xiaosheng Huang, Adam Fennimore and Chih-Wei Chang, Chris Regan, Shaul Aloni and Weiqiang Han, have created an cozy research environment. William Mickelson's Chinese certainly has livened up the computer room atmosphere. Weiqiang is a great guy to work

with; I thank him for being a persistent nanotube provider. Finally, it has been a wonderful experience working with Michael Hadman and Kevin Jones. They are remarkable "undergrads".

I would like to acknowledge my dear friends. Je-Luen Li and Aaron Lindenberg. for their continuous support and warm friendship throughout my six years at Cal. Aaron's proofreading of manuscripts has been a tremendous help.

I owe all I have today to my parents. who have brought me up in a unique way which somehow. has worked out quite well with my personality. I especially thank them for supporting me coming to America. for now I have the opportunity to pursue my dreams.

Finally, I thank Sabrina Qwan. Noah Bodzin. and Aaron Lindenberg for proofreading the thesis.

Part I

Vortex Matter in BSCCO-2212

Chapter 1

A High Temperature

Superconductor, BSCCO

1.1 Introduction to Superconductivity

In 1911, Kamerlingh Onnes discovered the first superconductor, mercury, which superconducts at 4.19 K. Since then, people have been searching continuously for new superconductors with higher T_c. One obvious goal is to find a material that superconducts at room temperature. Among single-element superconductors, niobium has the highest T_c of 9.25 K. Superconductivity at 23.2 K was discovered in the binary compound Nb_3Ge in 1973 by Gavaler [1], and held the record of the highest T_c until 1986. In 1986, Bednorz and Müller discovered $LaBaCuO_4$, which has a T_c of 35 K [2]. Their discovery marks the beginning of the High Temperature Superconductors (high T_c) era. In 1987, $Y_1Ba_2Cu_3O_{7-\delta}$ (YBCO-123) was found with a T_c of 92 K [3] and in 1988, BiSrCaCuO and TlBaCaCuO

[7, 8] were found with T_c reaching as high as 110 K and 130 K, respectively. As of today, the record for T_c is 160 K for $HgBa_2Ca_2Cu_3O_8$ under pressure [9].

All of the above high T_c materials are cuprates, which contain copper oxide planes in their crystal structure. Typical cuprate materials include LaSrCuO, YBaCuO, BiSr-CaCuO and HgBaCaCuO. The superconducting transition temperatures of cuprates at atmospheric pressure range from $\sim$ 35 K in LaSrCuO to 138 K in HgTlBaCaCuO. YBCO-123 and $Bi_2Sr_2CaCu_2O_{8+\delta}$ (BSCCO-2212) are two of the most studied cuprate superconductors. My research focuses on the highly anisotropic high T_c cuprate, BSCCO-2212, which I will abbreviate as BSCCO.

1.2 $Bi_2Sr_2CaCu_2O_{8+\delta}$

The critical temperature T_c of BSCCO depends on the stoichiometry of Bi and Sr, and on the oxygen doping levels. By increasing the oxygen content level of a BSCCO sample, BSCCO turns from an antiferromagnetic material to a superconductor, then from a superconductor to a non-superconducting metallic material. In the superconducting phase. T_c can vary from 83 K to 93 K depending on the oxygen doping level [10]. As the oxygen content increases, a BSCCO crystal can go from an underdoped, to an optimally-doped. and finally to an overdoped sample.

Like all high T_c cuprates, BSCCO is structurally and electronically an anisotropic material. The anisotropy of high T_c materials is characterized using an anisotropy parameter

4

BiO

BiO

SrO

CuO$_2$

Ca

CuO$_2$

SrO

BiO

BiO

SrO

c

a
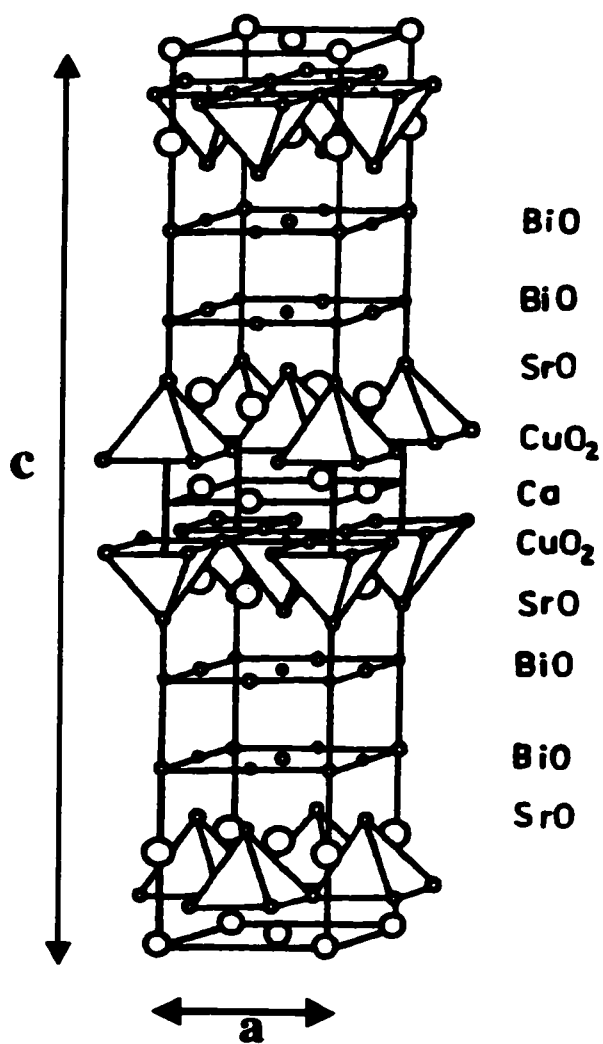
Figure 1.1: Crystal structure of Bi$_2$Sr$_2$CaCu$_2$O$_8$ (Beskrovnyi et al. 1990).

γ. γ is expressed as follows:

$$\gamma \equiv \left(\frac{m_c}{m_{ab}}\right)^{\frac{1}{2}} = \frac{\lambda_c}{\lambda_{ab}} = \frac{\xi_{ab}}{\xi_c}, \tag{1.1}$$

where m, λ, and ξ are the electron effective mass, penetration depth, and coherence length of the material. For m and ξ, subscripts ab and c refer to motion in the ab-plane and along the c-axis of the material, and for λ, refer to the direction of the screening supercurrent. γ is ~ 7 in YBCO and of order 100 in BSCCO. The exact value of γ in BSCCO is not certain: measurements have obtained γ values ranging from 55 [11] to 700 [12].

BSCCO has a tetragonal crystal structure. Figure 1.1 shows a primitive cell structure of BSCCO with the ideal oxygen stoichiometry of eight oxygen atoms per cell. The cell has unit vectors of $c = 30.7$ Å and $a = b = 5.4$ Å. Each primitive cell contains two pairs of CuO_2 double layers with Ca sandwiched in between both pairs of double layers. The CuO_2 double layers are separated from each other by a SrO/BiO/BiO/SrO multilayer with a thickness of 15 Å. The CuO_2 layers are believed to be the carrier planes for superconducting current, and the SrO/BiO/BiO/SrO layers the charge reservoir for the CuO_2 planes.

In BSCCO, the c-axis penetration depth at 0 K, $\lambda_{ab}(0)$, is ≈ 1500 Å and the ab-plane coherence length $\xi_{ab}(0)$ is ≈ 20 Å. With an average value of $\gamma \approx 200$, the c-axis coherence length $\xi_c(0)$ is estimated to be on the order of 0.1 Å. This value of $\xi_c(0)$ is shorter than the separation of the two CuO_2 layers of a pair, so a modified Ginzburg-Landau theory is necessary in calculating the properties of BSCCO. In general, the anisotropic Ginzburg-Landau theory and the two-dimensional Lawrence-Doniach theory are used in the phenomenological description of BSCCO in magnetic fields. The electron pairing mechanism in BSCCO has

been confirmed to have a d-wave symmetry, contrary to the spin-singlet s-wave symmetry in conventional low T_c superconductors.

Chapter 2

Introduction to Vortex Matter

2.1 Introduction

To discuss vortex matter properties in type-II superconductors it is necessary to introduce first the macroscopic Ginzburg-Landau (GL) theory. The GL theory gives a phenomenological description of superconductors in magnetic fields by introducing a complex order parameter $\psi(r)$, and $|\psi(r)|^2$ represents the density of superconducting electrons $n_s(r)$ at location r within the sample.

Ginzburg and Landau postulate that when the space variation of ψ is small in superconductors, the GL free energy density f of the superconductor can be expressed as

$$f = f_{n0} + \alpha|\psi|^2 + \frac{\beta}{2}|\psi|^4 + \sum_{\mu=1}^{3} \frac{1}{4m_\mu}\left|\left(\frac{\hbar}{i}\nabla_\mu - \frac{2e}{c}A\right)\psi\right|^2 + \frac{h^2}{8\pi}, \qquad (2.1)$$

where A is the vector potential. The first term of Eq. 2.1 is the normal state free energy density when the superconducting electron density $|\psi|^2$ is zero. The next two terms represent the condensation energy gained when the sample transits from the normal state to the

superconducting state. The fourth term represents energies associated with magnetic fields and gradients of the order parameter. The last term is the magnetic field energy density. $\mu = a, b$, and c represent the principal axes of a superconductor. For isotropic superconductors, $m_a = m_b = m_c$; for the anisotropic high T_c superconductor BSCCO, $m_a = m_b \gg m_c$ and Eq. 2.1 is the anisotropic GL equation. Here the mass m and charge e represent the mass and charge of one electron. In Eq. 2.1, $2m$ and $2e$ are used to represent the mass and charge of a cooper pair.

The minimization of the GL free energy density f with respect to ψ and A yields two important parameters: a penetration depth

$$\lambda_\mu = \left(\frac{2m_\mu c^2}{4\pi |\psi|^2 (2e)^2} \right)^{\frac{1}{2}} \tag{2.2}$$

and a coherence length

$$\xi_\mu = \left(\frac{\hbar^2}{4m_\mu |\alpha(T)|} \right)^{\frac{1}{2}}. \tag{2.3}$$

The penetration depth represents the characteristic decay length of magnetic field inside a superconductor. The coherence length describes the variation scale of ψ in space: it can also be thought of as the radius of a cooper pair.

The ratio of λ and ξ is κ,

$$\kappa = \frac{\lambda}{\xi}; \tag{2.4}$$

it is defined as the GL parameter.
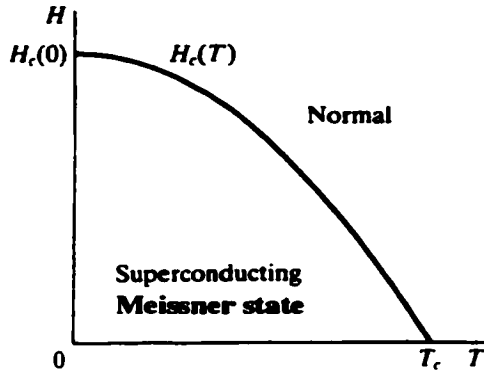
Figure 2.1: Type-I Superconductor.
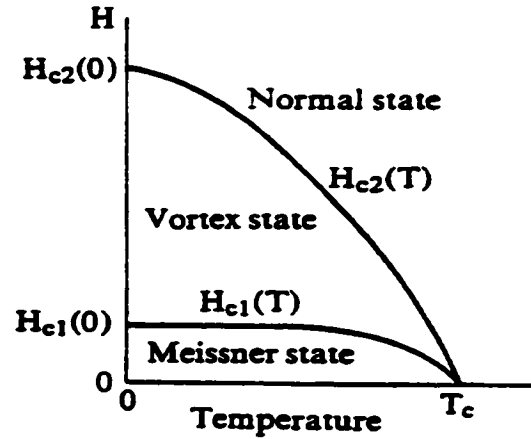
Figure 2.2: Type-II Superconductor.

2.2 Type-II Superconductors and Abrikosov Vortices

Superconductors can be sorted into two categories, type-I and type-II, according to their behavior in magnetic fields. The magnetic field and temperature phase diagrams for type-I and type-II superconductors are shown in Fig. 2.1 and Fig. 2.2. The value of κ determines whether a superconductor is a type-I or a type-II superconductor. When $\kappa < \frac{1}{\sqrt{2}}$, the sample is a type-I superconductor; when $\kappa > \frac{1}{\sqrt{2}}$, the sample is a type-II superconductor. BSCCO is an extreme type-II superconductor with $\kappa \gg \frac{1}{\sqrt{2}}$.

For type-I superconductors, a sample is in the Meissner state when the applied magnetic fields and temperatures are below the critical field line H_c as shown in Fig. 2.1. In the Meissner state, magnetic fields are fully expelled from the superconducting sample. Above H_c, the sample becomes normal and the magnetic field penetrates into the sample freely. All high-purity single-element superconductors are type-I superconductors.
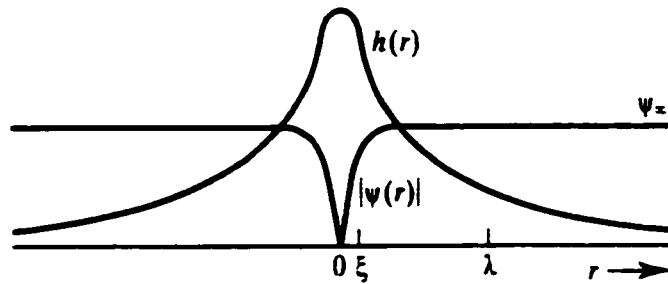
Figure 2.3: The structure of a vortex in a superconductor with $\kappa \approx 8$ (Tinkham, 1996).

For type-II superconductors, there is an additional vortex state in between the Meissner and the normal states. In the vortex state, individual magnetic vortices penetrate the sample. Abrikosov first predicted the existence of vortices in type-II superconductors in 1957. He [13] showed that in superconductors whose $\kappa > \frac{1}{\sqrt{2}}$, the surface energy is negative and single vortices penetrate through the sample like magnetic columns. Magnetic induction B ($B = H_a + 4\pi M$) only exists inside individual vortices. The areas outside the vortices are still diamagnetic ($B = 0$) and remain superconducting.

A vortex is a magnetic tube that penetrates through a superconducting sample. It is formed by circulating cooper pairs. The formation of a vortex makes no changes to the chemical composition and properties of a superconductor. Since the circulating electrons resemble the flow pattern of a vortex formed in a tornado or a bathtub, the magnetic column of circulating cooper pairs is also called a vortex. The magnetic flux through each vortex is quantized to be one flux quantum of

$$\Phi_0 = \frac{hc}{2e} = 2.07 \times 10^{-7} G - cm^2. \tag{2.5}$$

As opposed to isotropic superconductors, vortices in anisotropic superconductors

are called Abrikosov vortices only when they are parallel to the c-axis. The structure of an Abrikosov vortex in a superconductor with $\kappa \approx 8$ is shown in Fig. 2.3. The core of the vortex has a radius of ξ. In the center of the vortex core the sample is normal and the wave function of superconducting electrons $|\psi|$ is zero. Outside the core $|\psi|$ resumes its superconducting value. The local magnetic field density $h(r)$ is the highest at the center of the core and dies out at the penetration depth λ. For the rest of this thesis, the term vortex refers to an "Abrikosov vortex" unless otherwise noted.

Vortices repel each other via their supercurrent and magnetic field interactions. A vortex interacts with all its nearest neighbors. For infinite sample dimensions, the net repulsions are symmetric, and the net force on any given vortex is zero. The most stable vortex configuration in equilibrium is a triangular lattice configuration (a square lattice is an unstable lattice structure in equilibrium). Due to a numerical error, Abrikosov [13] had originally calculated the vortex lattice to be a square lattice. Later calculations [14] and magnetic decoration experiments [15] showed that the vortex lattice was triangular-shaped with a lattice parameter of

$$a_0 = 1.075 \left(\frac{\Phi_0}{B} \right)^{\frac{1}{2}}. \tag{2.6}$$

In type-II superconductors, the lower critical field H_{c1} separates the Meissner state from the vortex state, and the higher critical field H_{c2} separates the vortex state from the normal state. When the field near a superconductor reaches H_{c1}, it becomes energetically favorable for a vortex to form inside the sample. The penetration depth of the superconductor λ, which is also the radius of a vortex, is a relevant parameter in representing H_{c1}
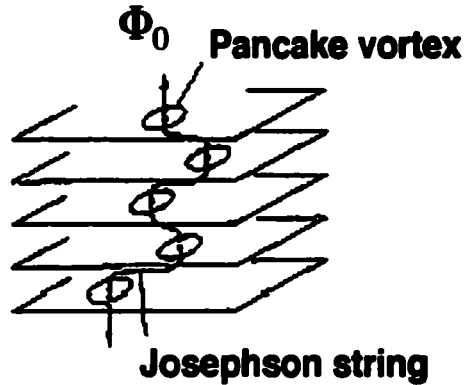
Figure 2.4: Pancake vortices connected by Josephson strings (Blatter et al., 1994).

as

$$H_{c1} = \frac{\Phi_0}{4\pi\lambda^2(T)} \ln\kappa.$$ (2.7)

H_{c1} essentially equals to one flux quantum divided by the area of one vortex, and therefore represents the average field distribution within the first vortex. As the magnetic field continuously increases, more vortices form in the sample. They pack more closely to each other until the field reaches H_{c2}. At H_{c2}, their cores start to overlap. At the upper critical field H_{c2}, a magnetic field fully penetrates into the sample and superconductivity is lost. H_{c2} relates to the vortex core radius ξ as

$$H_{c2} = \frac{\Phi_0}{2\pi\xi^2(T)}.$$ (2.8)

2.3 Lawrence-Doniach Model and Josephson Vortices

In extremely anisotropic superconductors such as BSCCO, magnetic properties are calculated using the two-dimensional Lawrence and Doniach (LD) model [16], which
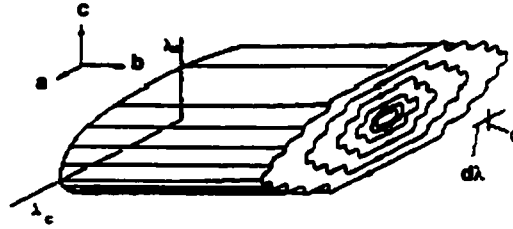
Figure 2.5: Structure of a Josephson vortex (Blatter et al., 1994).

assumes that a layered superconductor can be treated as a stack of discrete two-dimensional superconducting layers. The superconducting layers are separated by a distance d and couple to each other through Josephson tunneling. Within the LD model, an Abrikosov vortex is no longer a continuous straight column along the c-axis; instead it breaks into discrete vortex segments that reside in the superconducting layers. The segments are called pancake vortices. They connect to the neighboring layer pancakes by Josephson vortex strings in the interlayers. Figure 2.4 shows the Josephson string-connected pancakes. Josephson vortices in strongly layered cuprates are vortices formed in between the cupper-oxide layers when magnetic fields are parallel to the ab-planes of the sample. The structure of a Josephson vortex along the y-axis is shown in Fig. 2.5. Here the phase core of the Josephson vortex has the dimension of d and γd, and the field decays over a distance λ_c in the ab-plane direction, and $\lambda_{ab} = \frac{\lambda_c}{\gamma}$ in the c-axis direction. In contrast to an Abrikosov vortex, where the superconducting order parameter goes to zero in the core region, the superconducting order parameter in the phase core of a Josephson vortex is only weakly suppressed. Yet, the region outside the phase core is roughly identical to that of an Abrikosov vortex with circulating screening currents.

2.4 Current-Induced Vortex Dissipation

When a current is sent through a superconductor in the vortex state, vortices in the sample will experience a force due to the transport current. This force is called the Lorentz force. The Lorentz force density on the vortices is [17]

$$F = J \times \frac{B}{c},$$

(2.9)

where J is the current density and c is the speed of light. The force on a single vortex is then

$$f = J \times \frac{\Phi_0}{c}.$$

(2.10)

We can see from Eqs. 2.9 and 2.10 that the direction of the Lorentz force on the vortices is perpendicular to both the current and the magnetic field directions. Therefore, vortices move in the Lorentz force direction. If we use the crystal structure of BSCCO as an example, for a current applied along the b-axis and a magnetic field along the c-axis directions of the sample, vortices (or pancakes) will move along the a-axis with velocity v. As a direct consequence, an electric field of

$$E = B \times \frac{v}{c}$$

(2.11)

is generated by the moving vortex lattice. The direction of E is parallel to J. Vortex motion generated electric fields create dissipation inside a superconductor, which degrades the superconducting performance of the material.

Vortex generated dissipation is a major obstacle for realistic application of type-II superconductors. The main usage of type-II superconductors is to take advantage of their ability to carry high current densities without dissipation. High T_c superconductors are es-

pecially desirable because of their high values of H_{c2}. Since supercurrents passing through a superconductor generate magnetic fields of their own, if the fields exceed H_{c2} of the material, the superconductivity of the material is destroyed. Due to the high value of H_{c2} in high T_c materials, high T_c materials should theoretically enable the passage of high currents without being destroyed by their self-generated fields. However, the vortex-generated dissipation limits the current density a superconductor can carry. This troublesome vortex dissipation can be reduced or even eliminated only when the vortices are pinned down.

Vortices can move with the transport current freely when they are in the vortex liquid state. In the vortex solid state, vortices are collectively pinned by random pinning centers created by random inhomogeneities within the sample. The vortex motion is made possible by the assistance of thermal activation across the pinning energy barriers. This thermally assisted flux motion is called flux creep. Flux creep typically generates an Arrhenius type dissipation of $R \propto \exp(-\frac{U}{T})$, where U is the activation energy.

2.5   Vortex Matter Phases in BSCCO

2.5.1   Vortex Liquid, 2D and 3D Solid Phases

Because of the high superconducting transition temperature and the high anisotropy of BSCCO, the vortex matter in the mixed state of BSCCO is extremely complicated. Generally, the vortex matter can be separated into three phases: a liquid phase, a three-dimensional (3D) vortex solid phase, and a two-dimensional (2D) vortex solid phase. Figure 2.6 shows these three phases in the vortex matter phase diagram for BSCCO. The lower critical field H_{c1} is only of the order of 100 Oe in BSCCO, essentially zero on this scale.

The upper critical field H_{c2} is of order 100 T (at low temperatures), therefore it is almost vertical in Fig. 2.6 at high temperatures. The mixed state in between H_{c1} and H_{c2} contains vortex liquid, 3D vortex solid, and 2D vortex solid phases. The vortex liquid phase occupies the high temperature and high field regime of the vortex state, the 3D vortex solid phase occupies the low temperature and low field regime and the 2D vortex solid phase the low temperature and high field regime of the vortex state.

Now we explain the vortex matter phases in detail. A perfect vortex lattice has hexagonal symmetry with each vortex line at its fixed crystalline position. At high temperatures, thermal energy moves the vortices away from their ideal straight-line positions. There is a critical distance away from the equilibrium position that when the average motion of a vortex is above it, the vortex lattice is considered to be in a liquid phase. The wavy vortices are shown in the liquid phase of Fig. 2.6. Since the vibration motion is in all directions, a mean-square thermal vibration amplitude A^2 is introduced to express the displacement of a vortex as

$$A^2 = c_L^2 a_0^2, \tag{2.12}$$

where $c_L^2 \approx 0.15$ is the Lindemann parameter and a_0 is the vortex lattice spacing. When the mean-square thermal vibration amplitude A^2 is above $0.15 a_0{}^2$, vortices are considered to be in the liquid phase.

The mean-square thermal vibration amplitude A^2 of a vortex can be expressed as a function of temperature [17],

$$A^2 \sim \frac{\kappa T}{\sqrt{K \epsilon_1}}, \tag{2.13}$$

where $K \approx (\frac{\sqrt{3}\Phi_0}{r\pi^2\lambda^2})B$ is the restoring force constant per unit length of a vortex and $\epsilon_1 \sim$
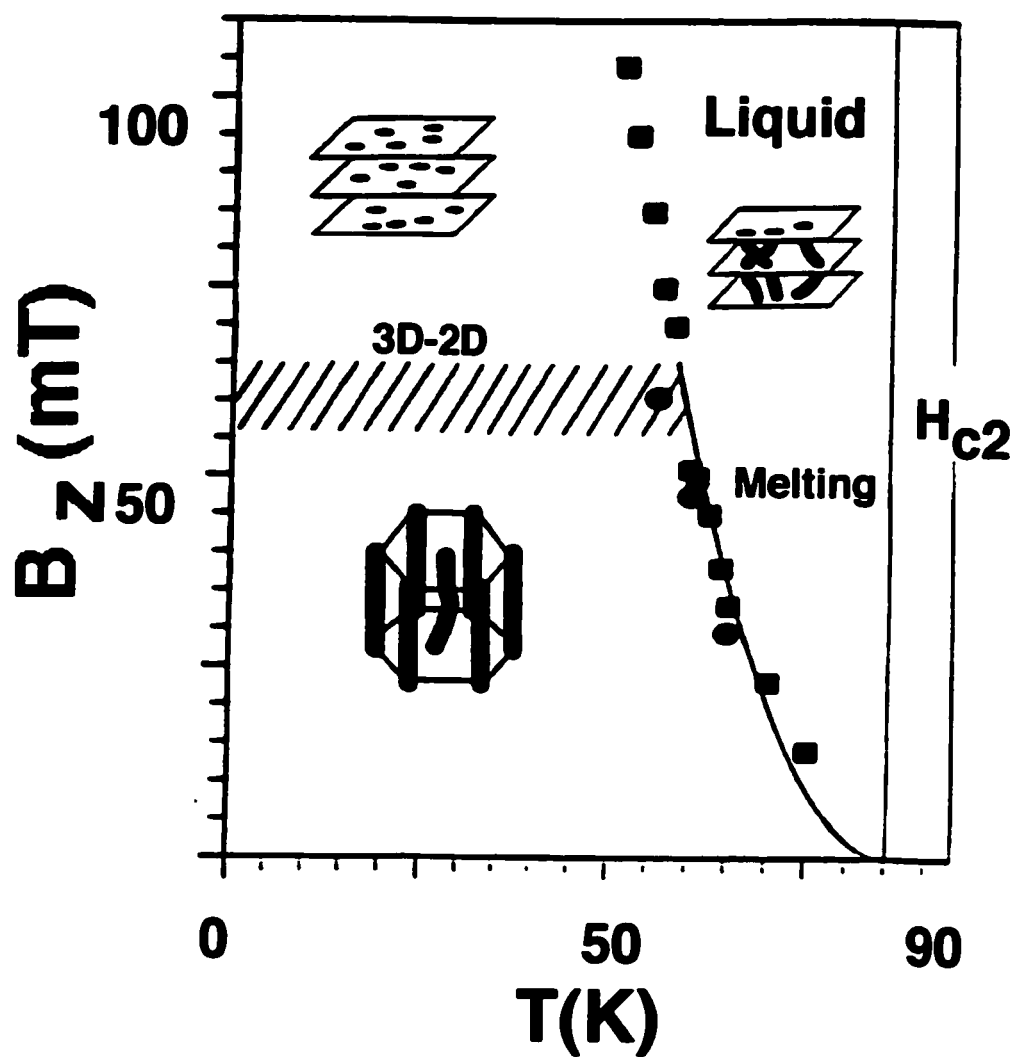
Figure 2.6: Vortex matter phase diagram of BSCCO (Cubitt et al., 1993 and Crabtree et al., 1997).

$(\frac{\Phi_0}{4\pi\lambda})^2$ is the vortex line tension. The vortex melting temperature T_m, which is defined as the temperature at which $A^2 = (0.15)^2 a_0^2$, can be obtained using Eqs. (2.12) and (2.13). The melting temperature therefore is a function of the magnetic induction B inside the sample [17]:

$$\kappa T_m = \frac{C c_L^2 \Phi_0^{\frac{5}{2}}}{\lambda^2 \sqrt{B}}, \tag{2.14}$$

where C is a constant. Figure 2.6 shows this B_z vs. T plot of the vortex melting transition line in BSCCO.

At fields and temperatures below the melting line, vortices form a nearly perfect triangular lattice as shown in Fig. 2.6. They are in the 3D vortex line solid phase. In this phase, random pinning centers in the sample pin the vortex lattice collectively and the symmetry of the vortex line lattice is little affected. This situation changes when the 3D vortex lines dissociate into 2D vortex pancakes at high fields and low temperatures. In the 2D vortex solid phase, pinning effects are non-negligible.

To fully understand the pinning effects in the 2D vortex solid phase, we need to explain first how a 3D vortex line lattice dissociates into 2D vortex pancakes. In an extremely layered superconductor such as BSCCO, a vortex line can be considered as a stack of pancake vortices threaded together along the direction of the applied field. The pancakes interact with each other through inter- and intra-layer interactions. When the vertical inter-layer interaction (mainly Josephson coupling) is stronger, the pancakes form a vortex line and the vortices are in the 3D phase. When the lateral in-plane pancake interaction is stronger, pancakes in each plane are dissociated from pancakes in neighboring planes and vortices are in the 2D state. Since the vertical pancake inter-layer interaction

is independent of B and the lateral intra-layer interaction is proportional to B, a crossover field at which the lateral interaction dominates can be obtained. The crossover field is a function of the anisotropy parameter γ as [18, 17]

$$B_{cr} \sim \frac{\Phi_0}{s^2\gamma^2}. \tag{2.15}$$

From Eq. 2.15, one can see that B_{cr} is independent of temperature. This temperature independent vortex solid 3D-2D phase transition line is shown in Fig. 2.6. Cartoon images of the dissociated 2D pancake lattices at high fields and the correlated vortex line lattice at low fields are also shown.

2.5.2 Vortex Matter Phase Transitions

Vortex matter phase transitions, which include primarily the vortex lattice melting transition and the vortex solid 3D-2D transition, have been studied extensively in BSCCO. The melting transition has been predicted [19] and detected using a variety of measurement techniques that include transport measurements [20], neutron diffraction studies [18], specific heat measurements [21] and local magnetization measurements [22]. The melting transition in BSCCO has been suggested to be first order [23]. This first-order nature was confirmed most convincingly by the observation of a latent heat at the melting transition in both the local magnetization and specific heat measurements [22, 21]. The vortex 3D-2D solid transition was calculated [24, 17] and probed mainly using neutron diffraction [18] and local magnetization methods [1]. Currently, the order of this vortex solid phase transition is still under debate, although recent local magnetization [25] and Josephson Plasma Resonance measurements [26] favor the first-order nature of the transition. In a later part of the thesis,
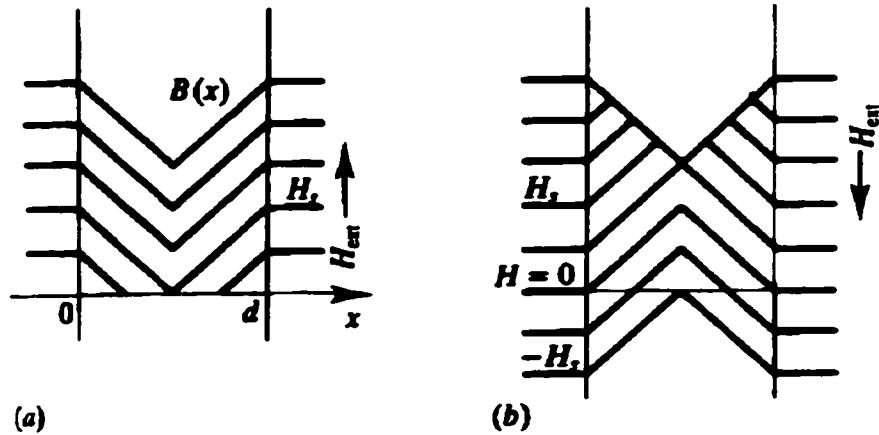
Figure 2.7: Bean flux-density profile in an infinite type-II superconducting slab in (a) increasing field and (b) decreasing field (Tinkham, 1996).

we will discuss how sample size influences the vortex matter phase transitions in BSCCO [27].

2.6 Bean Model

Magnetization in type-II superconductors is hysteretic and the flux-density distribution inside samples is inhomogeneous. These phenomena can be explained using the Bean magnetization Model [28], which postulates that all screening currents inside superconductors have the same field independent value of J_c. In changing magnetic fields, screening currents are created inside the superconducting sample to oppose the variation of the magnetic field. This screening current itself produces magnetic field, which together with the external magnetic field, creates an inhomogeneous flux-density profile within the sample.

Figure 2.7 illustrates the flux-density profile within an infinitely long slab of thickness d in an external magnetic field parallel to the plane of the slab, calculated using the

Bean model. As the field is increased, flux-density $[B(x)]$ decreases linearly from the sample edges into the center with a slope of $4\pi J_c/c$ [Fig. 2.7(a)] [28, 17], where J_c is the critical current and c the speed of light. The highest field the current can screen out from the center of the slab is H_s. At H_s, vortices penetrate fully into the slab. When the field is decreased. the flux is trapped inside the sample until a reversed field of $-H_s$ is reached as shown in [Fig. 2.7(b)]. As is evident from Fig. 2.6, the magnetization in type-II superconductors is hysteretic. We show here the flux-density profile inside an infinite slab. For samples with different shapes, the flux-density profiles can be very different. The Bean flux-density profile inside the highly anisotropic BSCCO is even more complicated.

In order to study the flux-density profile within a type-II superconductor, magnetic induction B inside the sample needs to be measured locally using a small probe. A local Hall sensor became the ideal tool for this task. E. Zeldov is one of the main developers of the GaAs/AlGaAs Hall sensor technique for studying local vortex behaviors in high T_c superconductors [29]. To obtain the flux-density distributions in many regions of a sample simultaneously, an array of closely packed local Hall sensors has been proven a powerful probe [30]. Two chapters of my thesis describe local magnetization measurements of BSCCO using a GaAs/AlGaAs Hall sensor.

2.7 Surface Barriers

In type-II superconductors, the lower critical field H_{c1} separates the Meissner state from the vortex state. At H_{c1}, the formation of vortices becomes energetically favorable. However, when a vortex tries to enter the sample, it encounters additional energy barriers
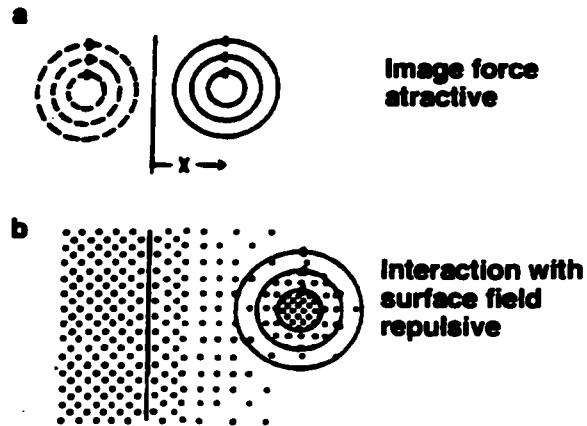
Figure 2.8: (a) Attractive force from the image vortex and (b) repulsive force from the surface field on the vortex (Bean, 1964).

created by the sample's boundary. The energy barriers against the entering vortices consist of a geometrical barrier [31, 29, 32], a Bean-Livingston (BL) surface barrier [33, 34, 35], and a bulk-pinning energy barrier [36, 28]. The geometrical barrier and the BL surface barrier together are called surface barriers.

We first describe the BL surface barrier effect. In 1964, Bean and Livingston proposed that to keep the boundary condition of zero current normal to the surface, a vortex near the sample surface should have an image [33]. The image vortex has the opposite sign. Figure 2.8(a) shows the image vortex. The force between the vortex and its image is attractive. At the same time, if the field direction is the same as that of the vortex thread, the surface field repels the vortex inwards [Fig. 2.8(b)]. These two forces on the vortex compete with each other. The image attractive force is a function of the vortex distance to sample edge x, and the repulsive force is a function of both x and the magnetic field H. The competition of the two forces leads to an energy-barrier profile for incoming vortices. This energy barrier for a cylindrical-shaped type-II superconductor is shown in Fig. 2.9.
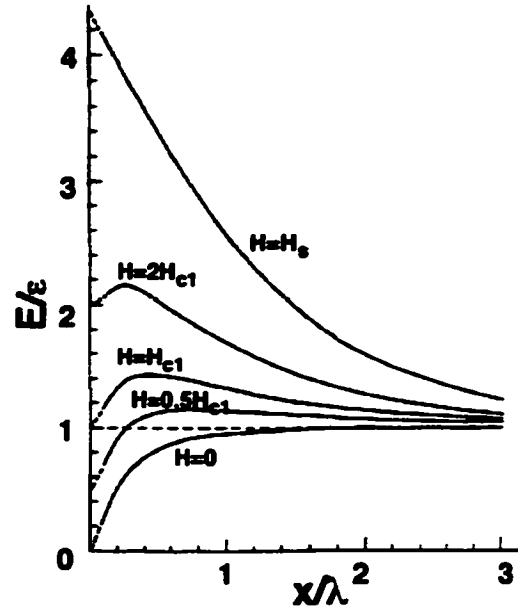
Figure 2.9: Vortex line energy E vs. distance x from the sample edge at different fields (Bean, 1964).

where the vortex line energy E vs. x is plotted for different magnetic fields. $\epsilon = \frac{\Phi_0 H_{c1}}{4\pi}$ is the vortex line energy at H_{c1}, the field at which a vortex becomes energetically favorable to form inside the superconductor neglecting the surface barrier effects. Notice that only at a higher applied field H_s does the BL surface energy barrier disappear for a vortex. In a later chapter, we will describe our measurements of the BL surface barrier effect in micron-sized BSCCO [37].

Now we discuss the geometrical barrier effect. When a vortex tries to enter a sample from the edges, the top and bottom surface shielding currents bend the top and the bottom segments of the vortex line inwards. Simultaneously, the vortex line tension tries to spring back the bent vortex to its original straight-line geometry. The competition of the two forces results in a sample-geometry-dependent energy barrier against incoming vortices.
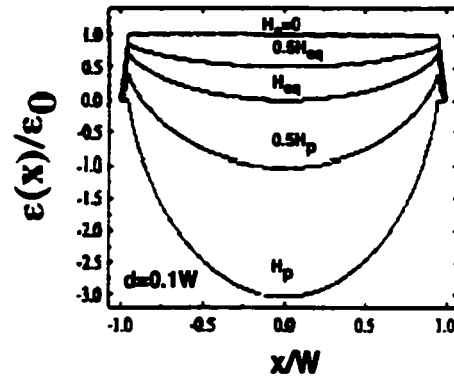
Figure 2.10: Vortex potential across a strip-shaped sample of width W (Zeldov. 1994).

Figure 10 shows the potential a vortex "feels" when entering a BSCCO strip of width W

at fields H_a lower than the vortex penetration field H_p. Only at fields higher than H_p does

the geometrical energy barrier vanish and vortices penetrate into the sample freely.

Chapter 3

Preparation of BSCCO Crystals

3.1 Single Crystal Growth

Single crystals of BSCCO are grown using the floating zone method [37]. We use crystals grown at University of Tokyo (Tamegai group) and National Institute of Advanced Industrial Science and Technology, Japan. In a typical crystal synthesis process, a BSCCO boule (usually 2 cm long and 50 mm wide) is first produced. A boule can be considered a large polycrystal of BSCCO, in which many millimeter-sized single crystals are embedded.

With a sharp scalpel and a pair of tweezers, we separate out large flat pieces of BSCCO from the boule. The pieces are typically one millimeter in size. BSCCO is a layered material, and the surface layers can be cleaved off using tape. We put a large BSCCO piece on a glass slide (without the use of gluing) and then cleave it until both sides are flat and shiny. At this point, the sample is usually much smaller and thinner than the original piece. The cleaved sample thickness typically ranges from 10 μm to 30 μm. Below 10 μm, the
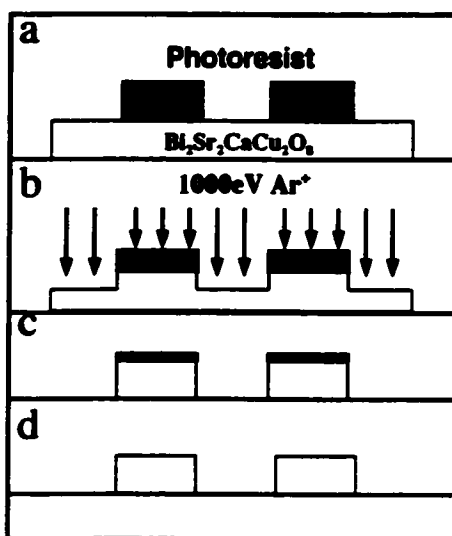
Figure 3.1: Schematics of fabricating micron-sized BSCCO. (a) Patterning photoresist on the sample surface. (b) BSCCO, together with the photoresist, is exposed to 1000 eV Ar$^+$ ion bombardment. (c) The Ar$^+$ bombardment stops when the sample is etched all the way through. (d) The remaining photoresist is dissolved away using acetone.

the crystal becomes too thin and can be easily damaged if it is further cleaved. If samples thinner than 10 μm are desired, the crystals should be etched using the ion-milling method to any desirable thickness within 10 μm.

3.2 Fabrication of Micron-sized BSCCO

The challenge of machining micron-sized BSCCO lies in the deep etching of small patterns. Previous methods using Ar$^+$-ionmilling and photolithography etch up to 10 nm in BSCCO at which point the photoresist begins to burn [38]. Deeper etching is harder to achieve with burned photoresist; in addition, the removal of the burned photoresist after etching is difficult. By introducing an annealing procedure before the ionmilling step, and using a thicker photoresist (Shipley 5740), we can consistently etch samples up to 10 μm
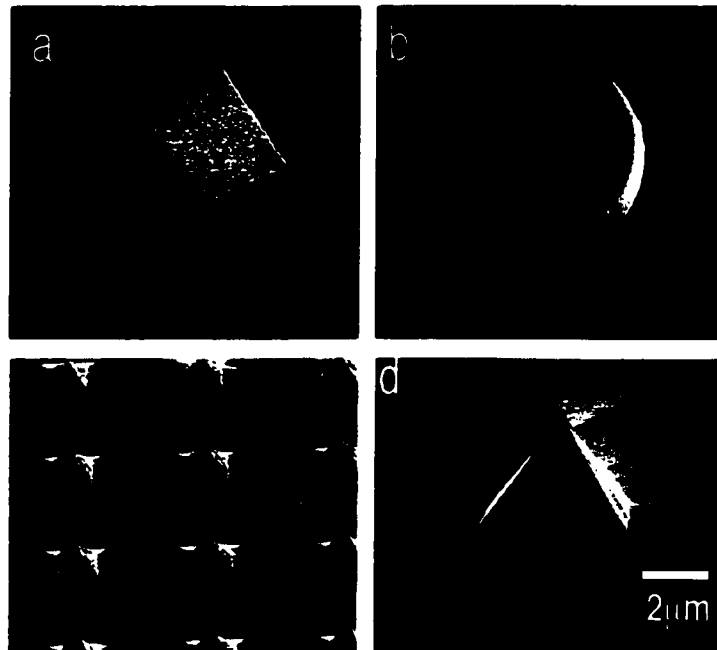
Figure 3.2: SEM image of a micro-machined (a) square, (b) disk, (c) pyramid array in BSCCO, and (d) a cone in silicon.

thick.

Figure 3.1 shows the schematic of the fabrication process. The photoresist pre-annealing step (30 min at 100°C) is applied after patterning the sample [Fig. 3.1(a)] and before starting the ionmilling process [Fig. 3.1(b)]. The pre-annealing prevents photoresist from burning during the milling process. The etch rate of pre-annealed photoresist is lower than that of BSCCO, enabling one to mill for hours until the 10 μm thick single crystal is completely etched through. BSCCO, together with the photoresist, is exposed to 1000 eV Ar$^+$ ion bombardment. The Ar$^+$ bombardment stops when the sample is etched all the way through. After the ionmilling, the pre-annealed photoresist is washed away using acetone [Fig. 3.1(c)] and the original smooth surface of BSCCO is restored [Fig. 3.1(d)].
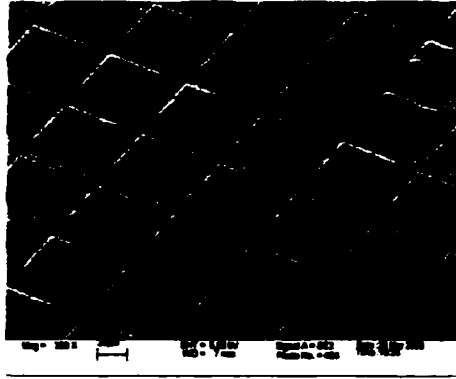
Figure 3.3: Array of 50×50 μm^2 photoresist squares.
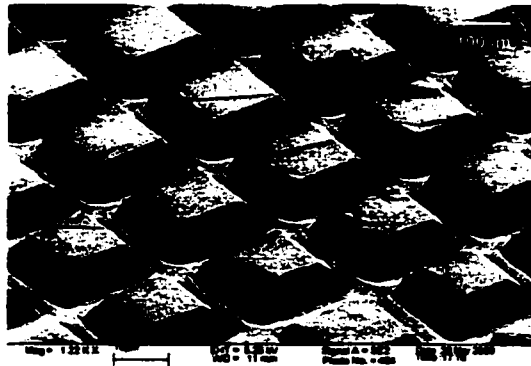
Figure 3.4: BSCCO Mesa array.

Figs. 3.2(a) and 3.2(b) show an ionmilled BSCCO square and disk, respectively. We note that by varying the size and shape of the photoresist, novel structures may be created in a range of materials, such as a pyramid array in BSCCO [Fig. 3.2(c)], and a cone in silicon [Fig. 3.2(d)].

The cone shapes illustrated in Figs. 3.2(c) and 3.2(d) are fabricated using a unique photoresist annealing process. In a normal micro-fabrication process, developed photoresists
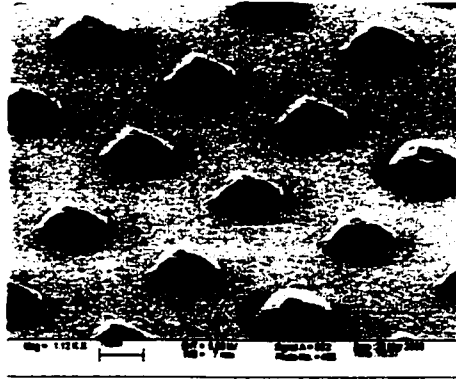
Figure 3.5: Array of 10×10 μm^2 square-shaped photoresist.

have a small edge profile as shown in Fig. 3.3. When this photoresist is used as a mask for ionmilling samples, the thinner edges of the photoresist are milled through first. Consequently, when the sample is etched through later, it will also have a side profile. BSCCO Mesa array structures etched using this method are shown in Fig. 3.4 (this Mesa-array-structured BSCCO sample has been used to study the sample size effect on vortex matter in BSCCO using Josephson Plasma Resonance measurements [40]). notice the side profiles of each Mesa. If the photoresist shrinks down to below 10 μm (Fig. 3.5), then the resist is nearly pyramid-shaped after the developing process. After further annealing, the edges of the resists smooth out and round dome-shapes form as shown in Fig. 3.6. The cones in Figs.3.2(c) and 3.2(d) are micro-fabricated using those small dome-shaped photoresists as masks.

Figure 3.6: After the annealing process, round photoresists become dome-shaped.

3.3 Fabricating Micron-sized Contacts onto BSCCO

In order to perform transport measurements in millimeter-sized BSCCO crystals, contact pads frequently need to be micron-sized to fit onto the small sample. Simple contacts, for example the conventional four-dot contact pattern for four-probe measurements, can be drawn by hand onto the BSCCO surface using silver paint. However, when the contact geometry becomes complicated, microfabrication techniques provide the best solution. Figure 3.7 shows micro-fabricated gold contacts on BSCCO. The ring and arcs on the right and the four bars on the left are two sets of four-probe contacts.

The procedure of fabricating the best contacts for transport measurements (contacts with good adhesion to sample surface and low contact resistance) is as follows: (a) Use Stycast epoxy (2850FT) to anchor a freshly cleaved BSCCO sample onto a substrate (typically sapphire) at four corners. (b) Evaporate gold ($\approx$ 2000 Å) onto the whole chip, which includes the sample, the Stycast and the substrate. (c) Pattern and develop the desired contact shapes onto the sample using photo-lithography as shown in Fig. 3.1(a).
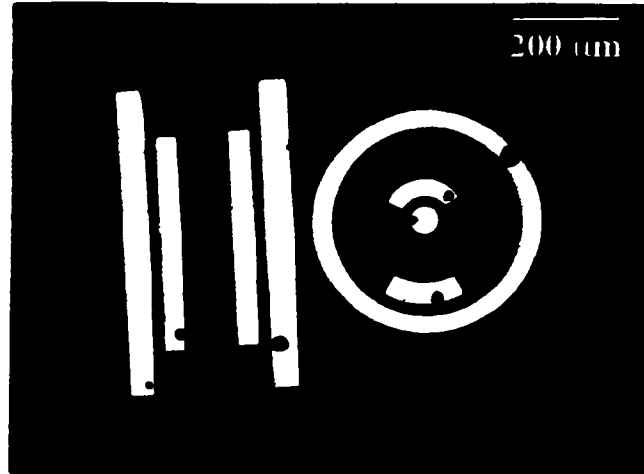
Figure 3.7: Micron-sized gold contacts on BSCCO.

(d) Anneal the photoresist at 90°C for 20 min. (e) Ion-mill the gold away at the uncovered areas using the resists as the masking layer. (f) Wash away the photoresist. The last step is to anneal the contacts at a higher temperature to decrease the contact resistance. This step can be combined with the oxygen-annealing step discussed in the next section. The contacts in Fig. 3.7 have contact resistances of order 0.2 Ω per contact pair.

3.4 Annealing for Proper Oxygen Doping

In terms of the oxygen content level, a BSCCO sample can be an as-grown sample. an overdoped sample and an underdoped sample. Since T_c and the vortex matter properties of BSCCO depend on the oxygen doping level, we anneal our samples to achieve a proper oxygen doping level before measurements. Our BSCCO sample are typically overdoped by annealing in air for over 14 hours at an average temperature of $\approx$500°C.

We put BSCCO single crystals (or microfabricated BSCCO crystals glued on a sapphire chip with Stycast epoxy resin) in a small clean alumina boat, then we put the boat into a preheated oven. The temperature of the oven should be 550°C if a T_c of 87 K is desired or 450°C for a T_c of 81 K. The annealing time should be a minimum of 14 hours. After the annealing, the alumina boat is taken out of the oven. Since alumina boats usually take a long time to cool down, and a slow cooling time may affect the oxygen levels of the doped sample. We remove the samples while the boat is still hot and place them on a clean glass slide for the next step of sample preparation.

The annealing process also burns off the Stycast (which we use to glue the BSCCO samples on the substrate) and the sample now sits on the substrate freely. They are very light and can be easily blown away by the slight turbulence of breathing, so the samples should be handled with care and shipped in a closed container.

3.5 T_c Characterization

We use two methods to characterize the T_c of our superconductor samples: a transport measurement method and a SQUID (Superconducting Quantum Interference Device) magnetometry method.

In the transport measurement method, the electrical resistance of a sample is measured as a function of temperature using both dc and low frequency ac measurements (AC Resistance Bridge, 16 Hz). The superconducting transition temperature T_c is defined as the temperature at which the resistance drops to zero. Figure 3.8 shows an ac resistance vs. temperature curve of a BSCCO sample measured using Corbino disk geometry contacts and
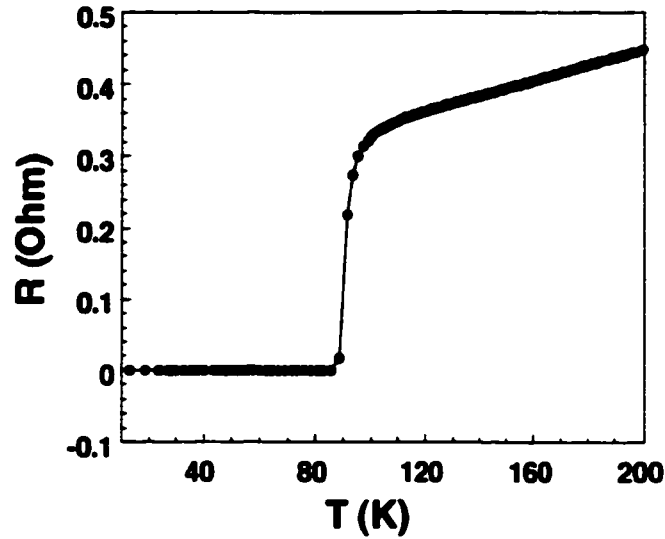
Figure 3.8: Determination of T_c using ac resistance measurements (16 Hz). T_c here is 93 K.

a current value of 1 mA. Normally, there is a temperature interval of ΔT for the resistance to drop from its normal value above T_c to the absolute zero. For the sample in Fig. 3.8, the temperature interval is $\approx$ 5 K. We take the temperature at the half-height of the resistance curve within ΔT as the superconductivity transition temperature; in this case, T_c is 93 K.

In the SQUID magnetometry method, we use a SQUID magnetometer manufactured by Quantum Design to measure the magnetization of our samples. We determine T_c from field-cooled and zero-field-cooled magnetization measurements. Figure 3.9 shows a SQUID measurement for a 2mm×3mm×20μm BSCCO single crystal. T_c is defined as the temperature at which both the zero-field-cooled and the field-cooled magnetizations start to drop. The irreversible temperature T_{irr} is defined as the temperature at which the two magnetization curves begin to split. For this sample, T_c is 90.5 K and T_{irr} is 88.5 K.
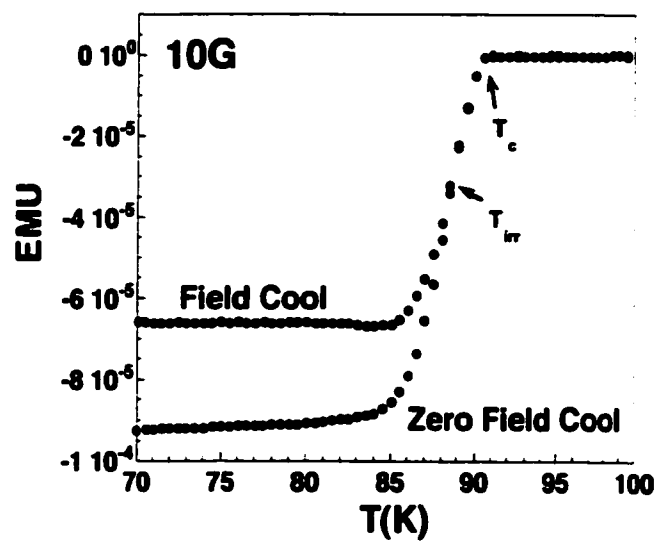
Figure 3.9: SQUID measurements of T_c and T_{irr}.

Chapter 4

New Vortex-matter Size Effect Observed in BSCCO

4.1 Background

Vortex matter, comprising the vortices in the mixed state of a high T_c supercon-ductor, is considered a model system for the study of phase transitions. The competition between three important energy scales (vortex-vortex interaction, pinning, and thermal) gives rise to a rich vortex matter phase diagram. At high temperature, thermal energy causes vortex lattice melting [22], while at low temperature, pinning can drive a transition of the vortex solid in layered anisotropic superconductors in which a three dimensional(3D) vortex line lattice dissociates into two-dimensional (2D) vortex pancakes with mainly ab-plane correlation [41, 18, 42]. The relevant parameters that determine the state of vortex-matter, temperature and applied magnetic field (analogous to pressure in atomic matter),

may each be varied independently over several orders of magnitude. In addition, the effects of tuning a wide range of materials parameters have been studied, such as disorder type and strength, anisotropy, and doping level. However, the effects of finite sample size on the state of vortex matter have received relatively little attention [43, 44]. Size effects, which have been important in the study of atomic matter phase transitions [45, 46], should also provide useful insight in the study of vortex matter. In addition, the richness of the vortex matter phase diagram offers the possibility of studying new size effects that have no atomic matter analogs.

In this chapter we investigate the effect of greatly reduced sample size on the disorder-driven 3D-2D vortex transition in BSCCO. Various models other than vortex solid 3D-2D transition have been proposed to explain the second magnetization peak (SMP) in BSCCO, including onset of vortex entanglement [47, 48] and order-disorder phase transitions [49, 50]. In the rest of our discussion the term "vortex solid 3D-2D phase transition" is used to collectively represent also these models for the SMP, the signature of a vortex-solid structural phase transition.

At low fixed temperatures, we find through local magnetization measurements that the SMP, the signature of a possible vortex solid 3D-2D transition, disappears for samples smaller than a temperature-dependent critical length. Existing models of the SMP are unable to account adequately for our observations. We suggest instead that the observed critical length R_{cr} reflects the 2D vortex lattice ab-plane correlation length R_c^{2D}. For samples smaller than R_c^{2D} the vortex lattice becomes insensitive to the disorder potential, and the disorder-driven vortex 3D-2D phase transition is absent. The magnitude and temperature
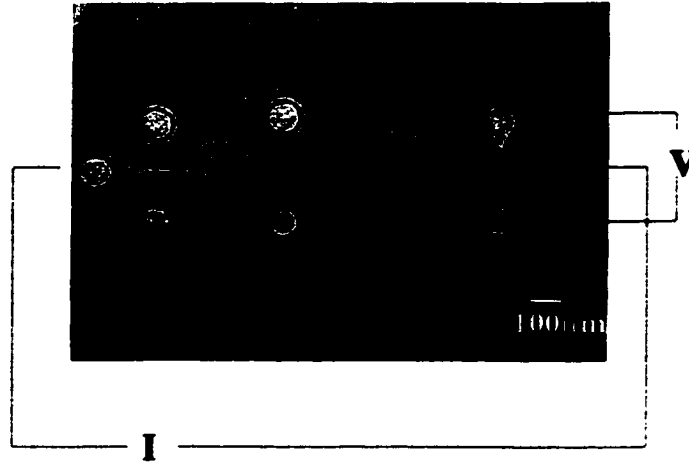
Figure 4.1: GaAs/AlGaAs Hall sensors device.

dependence of R_{cr} agree with R_c^{2D} in the Larkin-Ovchinnikov collective pinning model [51]. This correlation-length-driven size effect represents a new size effect mechanism in the vortex state.

4.2 Experiments

4.2.1 Experimental Set-Up

Single crystals of BSCCO were grown using the floating zone method [38]. The crystals were cleaved into 10 μm and 4.5 μm thick pieces. Disks and squares of lateral dimensions ranging from diameter $D = 30$ μm to 180 μm were then micro-fabricated from these pieces using photolithography and Ar-ionmilling. The samples were slightly overdoped ($T_c = 87$ K) after the fabrication by annealing in air at 550°C for 20 hours. The local magnetization of the samples was determined by placing the samples in a superconducting solenoid
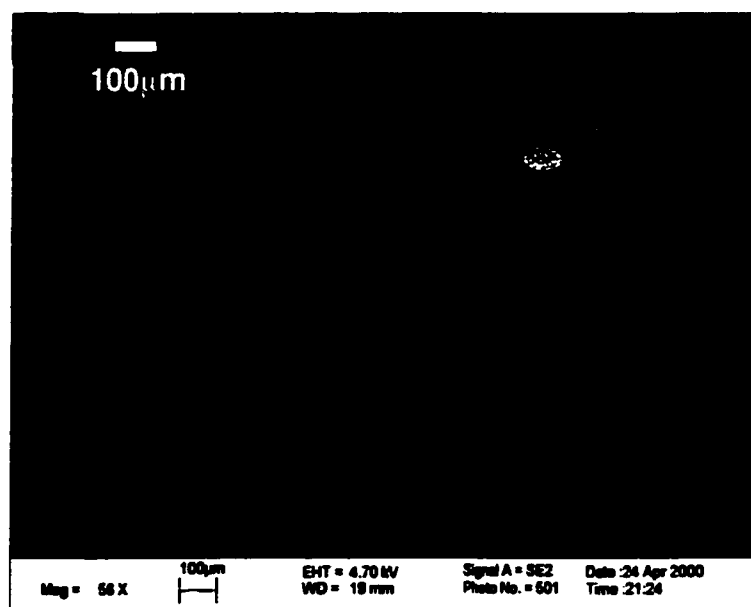
Figure 4.2: SEM image of the whole sensor device with two BSCCO disks mounted in place on two of the sensors.

with the applied field H_a parallel to the crystal c-axis. All local magnetization measurements were taken at the face center of the sample using a microfabricated GaAs/AlGaAs Hall sensor [22]. Figure 4.1 shows a whole Hall sensor device that contains three independent Hall sensors. Currents (typically 10 μA dc or ac) are applied through the two horizontal end contacts and Hall voltages are measured simultaneously at the three pairs of vertical contacts. One of the three sensors is used for calibration against magnetic fields, the other two can be used to measure two BSCCO samples simultaneously. Figure 4.2 shows a SEM image of the whole device with two BSCCO disks mounted in place on top of two sensors. A close up of the Hall sensors is shown in Fig. 4.3. This sensor has an active area of 10×10 μm^2. The BSCCO disk has diameter of 93 μm and thickness of 4.5 μm.

What is the advantage of using small local Hall sensors over SQUID magnetome-
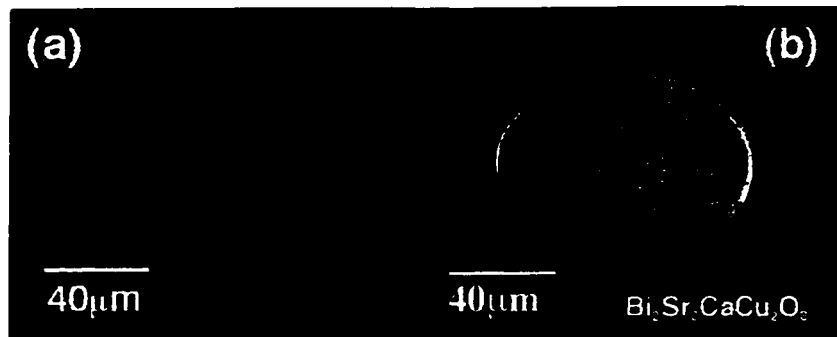
Figure 4.3: Zoom in of a Hall sensor (a) with no sample and (b) with a BSCCO disk mounted on top of the Hall sensor.

ters? The answer lies in the fact that SQUID magnetometers measure the global magnetizations of the whole sample. Due to pinning and surface barrier effects, flux-density distribution inside a type-II superconductor is not uniform. Therefore, global magnetization measurements are insufficient to elucidate the local flux-density profile within a sample. Only local magnetization measurements performed using a Hall sensor can provide this precise information.

Local magnetization measurements on zero-field-cooled samples were made at a magnetic field ramp-rate of 1 G/s for both increasing and decreasing fields. As a test of time-dependent effects, for one sample the ramp-rate was varied from 0.01 G/s to 20 G/s with no obvious differences in the magnetization.

4.2.2   Characterization of a GaAs/AlGaAs Hall Sensor

A GaAs/AlGaAs Hall sensor is characterized by measuring the Hall resistance R of the sensor as a function of the applied magnetic field. Hall resistance relates to Hall voltage as $V_H = RI$, where I is the applied current. Figure 4.4 shows the Hall resistance
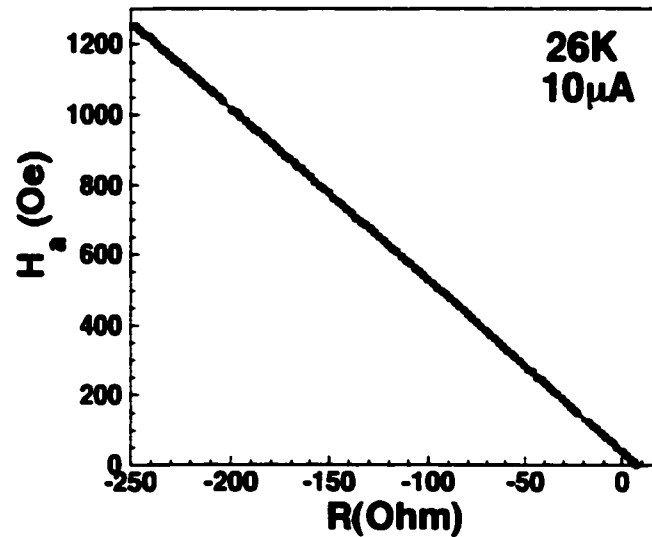
Figure 4.4: R vs. H_a of a Hall sensor at 26 K.

R vs. magnetic field H_a of a bare Hall sensor. The curve is a straight line and the slope of the line defines the coefficient of the Hall sensor. We use this Hall sensor coefficient later in data analysis for conversion of resistance value to local flux-density. When a BSCCO sample is mounted on top of a sensor, the sensor measures the local magnetic induction B of the sample (which is also the local flux-density). We apply an ac current of 10 μA to the sensor. This current density is reaching the limit of the maximum allowed current for our sensor area of $10 \times 10 ~\mu m^2$. Higher current densities run the risk of burning up the Hall sensor. With a nano-voltmeter, our Hall sensor is enable to detect magnetic fields as low as 5×10^{-4} G. For the sensor area of $10 \times 10 ~\mu m^2$, it is able to detect one-tenth of a single vortex.
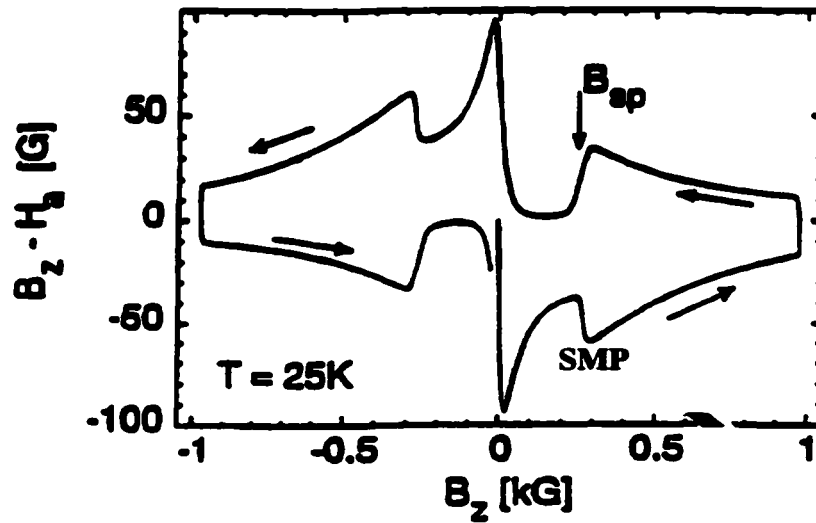
Figure 4.5: The Second Magnetization Peak in a large BSCCO sample taken from Ref. [1] (Khaykovich et al., 1996).

4.3 Detecting the Second Magnetization Peak

Figure 4.5 shows a typical local magnetization measurements of the SMP in a large BSCCO sample. The SMP is the sudden magnetization onset in the $B_z - H_a$, vs. B_z curve as denoted by B_{sp} in the decreasing field and by SMP in the increasing field. In our experiments, various micron-sized BSCCO samples were studied for SMP variations.

Figure 4.6 compares the local magnetization, $B_z - H_a$, vs. B_z for two different size BSCCO disks at two selected temperatures, 25 K and 30 K. H_a is the applied field parallel to the c-axis of BSCCO, and B_z is the local magnetic induction as determined by the Hall sensor. The two disks have diameters D of 70 μm and 30 μm, and thickness t of 10 μm and 4.5 μm, respectively. The most striking feature of Fig. 4.6 is that the SMP, as denoted by the arrow at $\approx$550 G in the 70 μm disk data, is absent in the 30 μm disk at both temperatures. From Fig. 4.6 we infer that at both 30 K and 25 K the critical lateral

size R_{cr} at which the SMP disappears lies somewhere between 70 μm and 30 μm.

4.4   The SMP Changes with Sample Size

In order to determine accurately R_{cr}(T), magnetization measurements for a given

sample were repeated at a series of fixed temperatures. Figure 4.7 shows representative data

for a different BSCCO sample, in this case a 90 μm square with $t = 10\mu$m. For this sample

the SMP is observed only at temperatures somewhat below 38 K, again at a temperature

independent B_z of 550 G. B_z is consistent with the previously published SMP field B_z of

macroscopic overdoped BSCCO samples [1]. We thus find that when the SMP is observed

at all in small BSCCO samples, it occurs at the same magnetic induction as that for larger

samples. Figure 4.7 shows that as the temperature is increased, the SMP anomaly becomes

successively smaller. Above a (sample-size dependent) critical temperature T_{cr}, the SMP

disappears completely. In order to determine T_{cr} accurately, we plot the SMP peak height

(defined as the difference of the local hysteretic magnetization for magnetic induction just

before and just after the SMP anomaly) as a function of temperature, as shown in the

inset to Fig. 4.7. The peak height can be fit empirically with a logarithmic temperature

dependence indicating an abrupt trend to zero height at finite temperature. Extrapolation

of the peak height to zero defines T_{cr}. For the 90 μm sample of Fig. 4.7, the SMP disappears

definitively at 35 K. Hence, $R_{cr}(T = 35$ K)$= 90\mu$m.

We have repeated the measurements of Fig. 4.7 for eight different samples of differ-

ent size ranging from 30 μm to 180 μm, thus generally determining T_{cr}(R), or equivalently,

R_{cr}(T). Figure 4.8 shows the results, which define a new SMP phase diagram for BSCCO
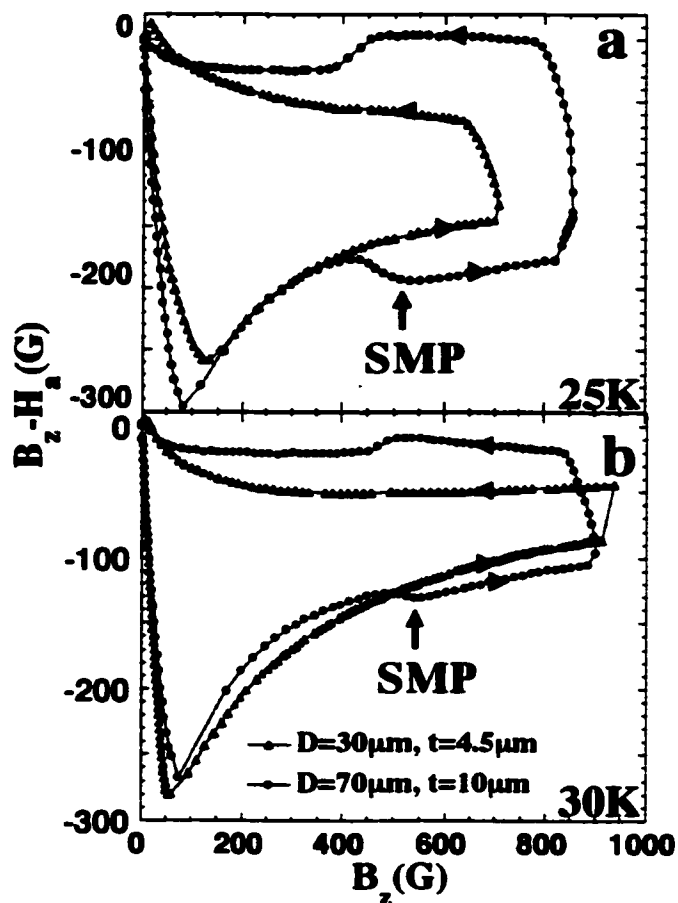
Figure 4.6: Local magnetization curves, $B_z - H_a$ vs. magnetic induction B_z at (a) 25 K and (b) 30 K for BSCCO disks with identical thickness-to-diameter ratio of $t/D \approx 0.15$.
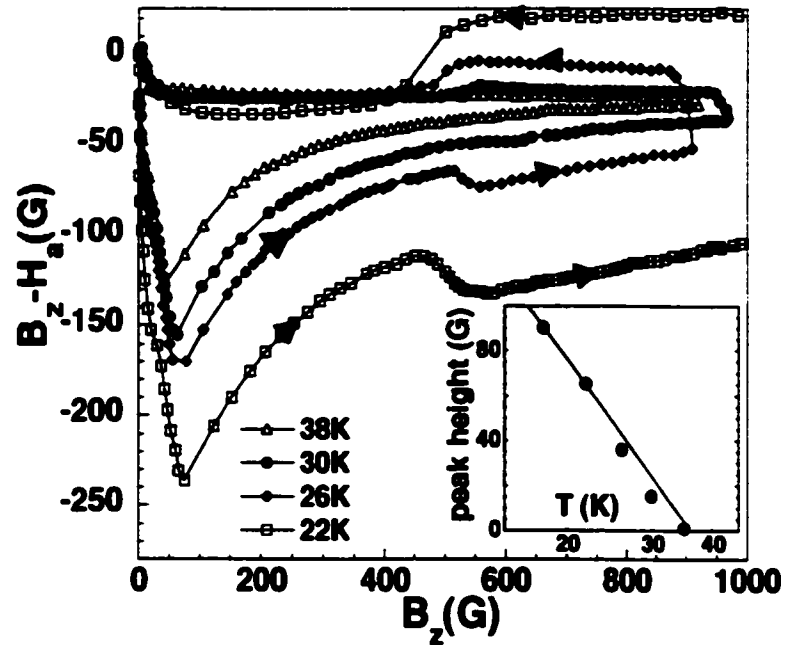
Figure 4.7: $B_z - H_a$ vs. B_z for a 90 μm square at selected temperatures. The inset shows the SMP peak height as a function of temperature on a logarithmic scale.

incorporating sample size. The temperature interval plotted is 20 K to 45 K. which is the relevant temperature interval for the SMP using local magnetization measurement [1]. All samples used for this plot are 10 μm thick. R_{cr} represents the diameter for a disk and the width for a square. Filled squares and circles represent measurements on square and circular samples, respectively. The line is a fit to the Larkin-Ovchinnikov ab-plane vortex correlation length $R_{cr} = (1.8\mu\text{m})\exp(T/9\text{K})$ [51]. We find no appreciable difference in the phase diagram between circular and square samples.
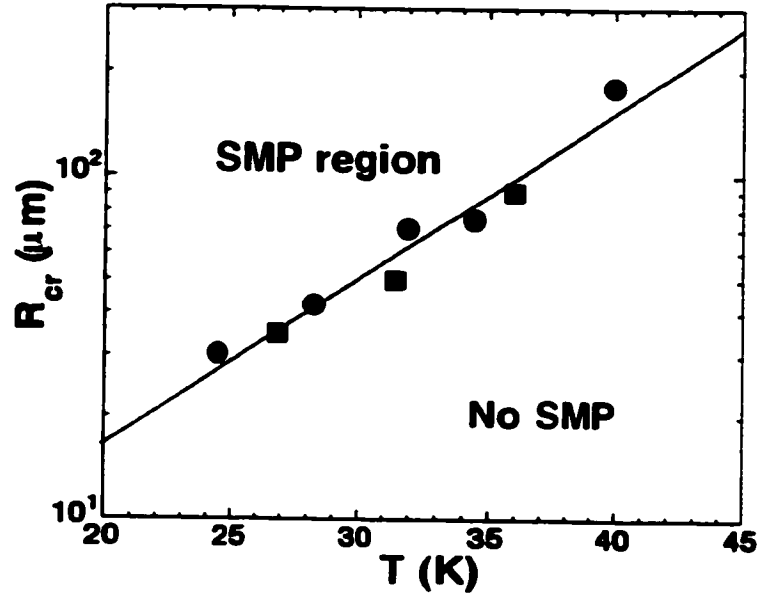
Figure 4.8: Critical sample size R_{cr}(T) below which the SMP is absent, shown as a function of temperature.

4.5 Analysis

We now discuss these results more fully. We first consider the expected geometry dependence of the various contributions to the total (measured) hysteretic magnetization. There are two mechanisms which give rise to hysteresis in the magnetization: one is bulk impurity pinning [28], which represents pinning of vortices by point disorder in the bulk of the sample; the other is surface barriers, which include the Bean-Livingston surface barrier [33] and geometrical barriers [29, 52]. The total local magnetization hysteresis is the sum of bulk pinning hysteresis $M_{bulk}(B_z)$ and surface barrier hysteresis $M_{barrier}(B_z)$ [35], where $M_{bulk}(B_z) = |(B_z - H_a)\uparrow - (B_z - H_a)\downarrow|$ with $\uparrow$ and $\downarrow$ representing ascending and descending field directions, respectively. Each pinning mechanism is expected to have a different dependence on sample dimension: $M_{bulk} \propto DJ_c$ according to the Bean model [28].

where J_c is the critical current density and D the sample diameter; and $M_{barrier}$ is expected

to be a function of the thickness-to-diameter ratio t/D for both Bean-Livingston surface

barrier and geometrical barrier [52, 35, 53, 54, 34]. Because $M_{barrier}$ increases and M_{bulk}

decreases as D decreases, the barrier magnetization overwhelms bulk magnetization in small

samples [55]. While the continuity of $M_{barrier}$ at the 3D-2D transition remains unclear [56],

ideally, samples of similar $M_{barrier}$ should be studied such that differences in M_{bulk} would

be evident.

For Fig. 4.6 we have in fact carefully chosen samples of similar thickness-to-

diameter ratios $(t/D{\sim}0.15$ for both samples) in order to achieve a similar value of $M_{barrier}$.

Confirming the theoretical prediction, the vortex penetration field H_p, defined as the value

of H_a at the first negative peak of the local magnetization, $H_a = B_z - (B_z - H_a)$, is in-

deed identical for both disks (with values $H_p{\approx}380$ G at 25 K and 330 G at 30 K). Thus

these two samples have the same value of $M_{barrier}$ above H_p, and the total hysteretic mag-

netization difference between the two disks is strictly the difference in the bulk pinning

magnetization—surface effects have been eliminated. It is thus instructive to further com-

pare the magnetization data of these two samples, as seen in Fig. 4.6.

Below the SMP, the total magnetization, and thus M_{bulk}, is narrower in the 30

μm disk, in agreement with the Bean model [28] where $M_{bulk}{\propto}DJ_c$. The 70 μm disk has

a magnetization jump at $B_z{\approx}550$ G, indicating a 3D-2D phase transition (not observed in

the 30 μm disk). It is believed that across the SMP line of the vortex phase diagram, a 3D

vortex-line solid dissociates into a randomly pinned pancake vortex solid. As the pancake

vortex solid, with its smaller correlated volume [51], can better adapt to the random pinning

centers, the critical current increases upon the transition from the 3D to the 2D state. The SMP signifies the increase of critical current since $M_{bulk} \propto DJ_c$. We expect that if the vortex 3D-2D transition exists in the 30 μm disk, the increase in J_c should be the same as in the 70 μm disk, and a magnetization peak of approximately 3/7 (30 μm/70 μm) the magnitude of that in the 70 μm disk should be observed. This is inconsistent with our observations. The absence of an observed peak in the 30 μm disk at temperatures higher than 25 K (Fig. 4.6) allows us to put an upper bound on the peak height of at least 10 times smaller than this estimate, indicating a dramatic suppression of the critical current increase associated with rearrangement of vortices at the 3D-2D transition. We can draw similar conclusions for our other sample sets.

4.6 Interpretations and the Larkin-Ovchinnikov Collective Pinning Model

What is the physical origin of the shrinking of the SMP line in very small BSCCO samples? Kopelevich and Esquinazi recently proposed vortex avalanches as a source of the SMP in BSCCO [43]. Their model suggests that in bulk BSCCO the heat generated by vortex motion cannot be dissipated fast enough due to the large lateral sample size. Sample heating lowers the energy barrier for vortex influx, which results in the SMP. In small samples, heat is released faster than its generation rate due to the short lateral dimension, and therefore the SMP may be absent. Unfortunately, this model predicts [43] a temperature dependence of R_{cr} at odds with our findings in Fig. 4.8.

Another possibility is that the shrinking of the SMP line in small samples is a
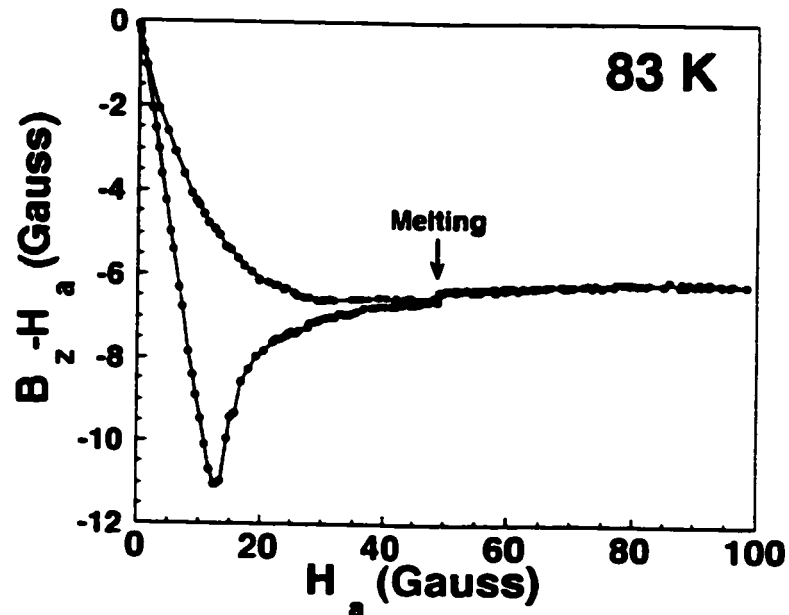
Figure 4.9: Vortex lattice melting transition is unaffected by sample size.

result of a sample-size-induced overall downward shift in temperature of the vortex lattice *melting* line and its associated critical end point. This is relevant since in BSCCO the vortex solid SMP line is connected to the vortex lattice melting transition line by the critical end point [22]. Since at $B_z \approx 550$ G, the ratio of the number of edge vortices to the bulk vortices reaches ~3% in the 30 μm disk, the phase transition in consideration may no longer be in the thermodynamic regime. If vortex lattice melting were indeed affected by the large surface-to-volume ratio of small samples (as in atomic matter melting), there could result a compression of the SMP line at low temperatures. We have tested this hypothesis by independently examining the sample size dependence of the vortex lattice melting line. Above $T = 60$ K, the melting onset field B_z(melting) and the magnitude of the melting jumps are independent of sample size and agree with reported results on over-doped BSCCO

[1]. Figure 4.6 shows the vortex lattice melting jump in the $B_z - H_a$ vs. H_a curve of BSCCO at 83 K. The melting jump can be clearly seen as denoted by the arrow. At low temperature (but still above the SMP temperature T_{cr}), the large barrier magnetization owing to small sample size obscures the observation of the small magnetization jump upon melting. Thus at present we cannot resolve the melting jump below $T = 60$ K. Thus, an overall downward shift of the melting line is ruled out as the origin of the shifting of the SMP.

We propose here a new model that accounts naturally for the SMP disappearance above T_{cr} in small samples. The SMP signifies an increase in bulk vortex pinning, and hence an increase in J_c, as the vortex lattice structure changes from 3D, with primarily out-of-plane vortex correlation, to 2D, with primarily in-plane vortex correlation. In the Larkin-Ovchinnikov (LO) collective pinning model the vortex lattice is treated as correlated within a volume defined by the ab-plane correlation length R_c, and the c-axis correlation length L_c. The vortex lattice may rearrange to lower its energy in the pinning potential only on scales larger than the correlation volume. The 3D LO correlation volume is shown in Fig. 4.10. Upon the conventional 3D to 2D transition, L_c decreases, while R_c increases. The net effect is an increase in the pinning energy of the 2D state, which favors its formation. However, the LO model should break down for samples with one or more dimensions smaller than the relevant correlation lengths.

In our samples for certain temperatures the lateral sample dimension becomes smaller than the 2D ab-plane correlation length R_c^{2D}. In this case, the 2D vortex lattice in each superconducting layer is correlated across the entire sample. The ability of the vortex lattice to rearrange in response to the disorder potential is reduced, and hence the 2D state
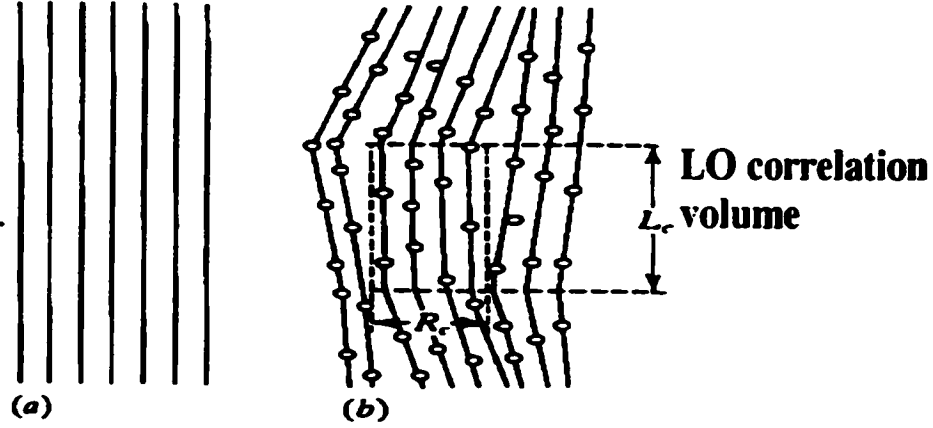
Figure 4.10: Larkin-Ovchinnikov 3D collective pinning model (Tinkham, 1996).

becomes less favorable energetically. Hence we expect a suppression of the 2D phase in samples smaller than the 2D ab-plane correlation length R_c^{2D}.

Our model may be tested quantitatively. We estimate the magnitude and temperature dependence of R_c^{2D} using the 2D LO collective pinning model [33, 51] in order to make comparison with the experimentally determined $R_{cr}(T)$. In the 2D LO collective pinning model the out-of-plane pancake vortex correlation length is taken as the interlayer distance, and the ab-plane correlation length is given as [17]

$$R_c^{2D} = \sqrt{\frac{C_{66}c}{J_c B_z \xi}} a_0,$$
(4.1)

where the shear modulus of the vortex lattice $C_{66} \approx B_z H_{c1}/16\pi$, the critical current $J_c(T) \approx J_c(0)\exp(-T/T_0)$ [54], ξ is the ab-plane coherence length, c is the speed of light, and the inter-vortex distance $a_0 = \sqrt{\Phi_0/B_z}$, with Φ_0 the superconducting flux quantum. The temperature dependence of R_c^{2D} comes primarily from the exponential temperature dependence of the critical current J_c; thus we expect an exponential dependence of R_c^{2D}

on temperature. If we assume reasonable values of $\xi = 2.5$ nm, $H_{c1} = 100$ G [57], and $J_c(0) = 5x10^5$ A/cm^2 [17], we find $R_c = (2.2\mu m)\exp(T/2T_0)$ at $B_z = 550$ G, where T_0 is the temperature exponent of the critical current, estimated to be of order 10 K in BSCCO.

The solid line in Fig. 4.8 is a fit of Eq. 4.1 to the experimental data, yielding $R_{cr} = (1.8\mu m)\exp(T/9K)$. The exponential temperature dependence agrees with the expected behavior of R_c^{2D}, giving a reasonable $T_0 = 4.5$ K for the critical current temperature exponent. The agreement in the prefactor is excellent, given the uncertainty in H_{c1} and $J_c(0)$.

In conclusion, we have investigated in detail using local magnetization measurements the effect of finite sample size on the SMP in BSCCO single crystals. We suggest that the 2D vortex lattice correlation length R_c^{2D} sets, at a given temperature, the limit for sample size below which the SMP, the signature of the vortex lattice 3D - 2D transition, is not observed. Complementary studies, such as neutron diffraction [18], would be highly desirable to further elucidate the vortex dimensionality in BSCCO samples smaller than R_c^{2D}.

Chapter 5

Vortex Penetration into

Micron-sized BSCCO

5.1 Introduction to Vortex Penetration

In type-II superconductors, the lower critical field H_{c1} separates the Meissner state from the vortex state. At H_{c1}, the formation of vortices becomes energetically favorable. However, when a vortex tries to enter the sample, it encounters additional energy barriers created by the sample's boundary. A magnetic field different from H_{c1} is required for a vortex to overcome these barriers. When the required magnetic field is higher than H_{c1}, a vortex penetration field H_p higher than H_{c1} is observed in experiments. Investigation of H_p should provide direct information concerning the energy barriers acting against the entering vortices, which in turn should lead to a better understanding of the vortex entry mechanism in type-II superconductors.

The energy barriers against the entering vortices consist of a geometrical barrier [29, 31, 32], a Bean-Livingston surface barrier [33, 34, 35], and a bulk-pinning energy barrier [36, 28]. The geometrical barrier and the Bean-Livingston surface barrier together are called surface barriers. Various models show that both the surface barriers and the bulk-pinning barrier vary with sample size and geometry, though differently because of their different origins. The geometrical barrier is caused by the competition between two forces on a vortex: the inward Lorentz force due to the Meissner shielding current and the outward force due to line tension [29, 31, 32]. It varies with the sample thickness-to-width ratio t/D [32, 53, 54, 58, 59]. The Bean-Livingston surface barrier, which is the result of the outward attractive force on a vortex by its image, also depends on t/D, though indirectly through the demagnetization factor [33, 34, 35]. The bulk pinning energy barrier is caused by point impurity pinning in the sample. It increases with the sample width D [36, 28]. By studying the variation of H_p with sample size and shape, one can experimentally obtain the sample geometry dependence of the above energy barriers.

In this chapter, we investigate the vortex penetration field H_p in BSCCO. The high anisotropy associated with BSCCO makes a study of H_p particularly desirable. However, experimental studies of H_p in BSCCO have been challenging due to the difficulty associated with fabricating small samples. In particular, the typical thickness of BSCCO single crystals is of order 10 μm and the surface barriers are functions of t/D. Thus, in order for t/D to be of order unity, the width of a sample must be micon-sized.
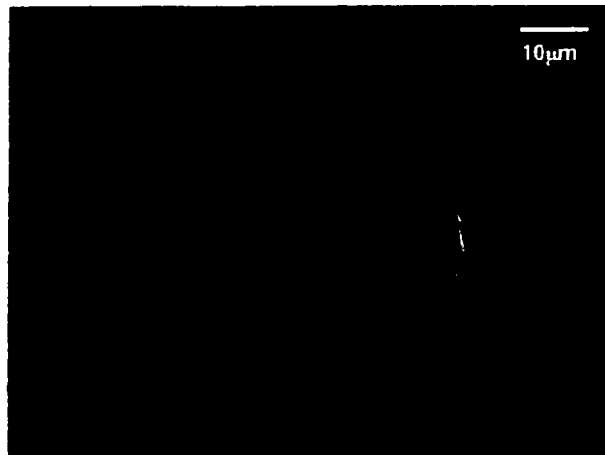
Figure 5.1: A 30 μm BSCCO disk mounted on top of a Hall sensor.

5.2 Experiments

We etched micron-sized BSCCO samples using the Ar-ionmilling method described in a previous chapter. For the present study, ionmilled samples of BSCCO were slightly over-doped ($T_c = 87$ K) after fabrication by annealing in air at 550°C for 20 hours. The local magnetization of the samples was determined by placing the samples in a superconducting solenoid with the applied field H_a parallel to the crystal c-axis. All local magnetization measurements were taken at the face center of the sample using the microfabricated GaAs/AlGaAs Hall sensor. Figure 5.1 shows a 30 μm disk on the Hall sensor. Local magnetization measurements on zero-field-cooled samples were made at a magnetic field ramp-rate of 1 (Oe/s) for both increasing and decreasing field.

Figure 5.2 shows the local magnetization, $B_z - H_a$ vs. applied field H_a at 30 K for 10 μm thick BSCCO disks with diameter D ranging from 20 μm to 180 μm, where B_z is the local magnetic induction. H_a at the first peak of the $B_z - H_a$ vs. H_a curve is defined as the
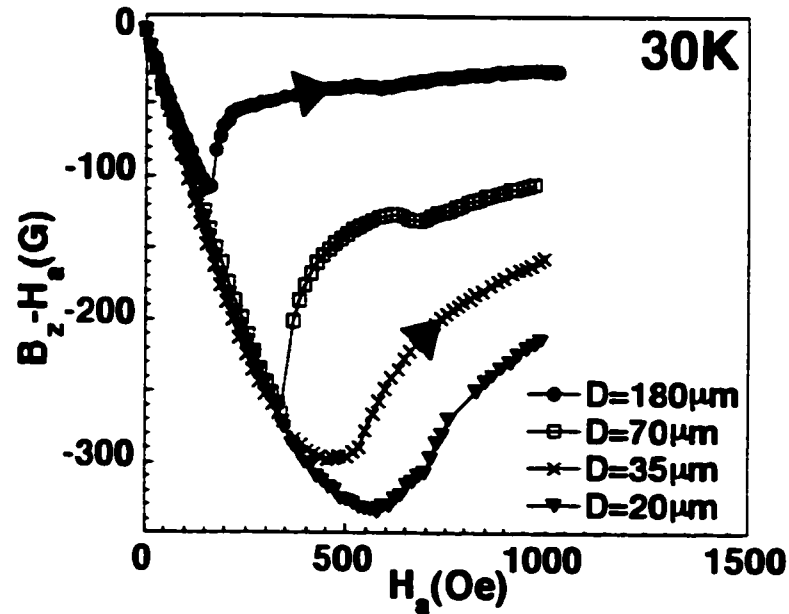
Figure 5.2: $B_z - H_a$ vs. H_a of BSCCO disks with diameter D of 20 μm, 35 μm, 70 μm, and 180 μm at 30 K.

vortex penetration field H_p. We attribute the early deviation from linearity of the 20 μm and 35 μm disks to the comparable size of the sample and the Hall sensor area. The arrowhead indicates the field-sweep direction. Since the Hall sensor is located under the center of the sample, the H_p reported here measures the full vortex penetration field, representing the magnetic field at which the vortices reach the center of the sample. As shown in Fig. 5.2, at 30 K H_p increases as the diameter of the sample becomes smaller. The measurements of Fig. 5.2 have been repeated for square- and disk-shaped samples at temperatures ranging from 5 K to 83 K. H_p exhibits distinctively different sample size dependences above and below 15 K.

Above 15 K, H_p decreases with sample size as a function of $\sqrt{t/D}$. Fig. 5.3 displays H_p vs. $\sqrt{t/D}$ for BSCCO (a) disks and (b) squares at selected temperatures above 15 K.
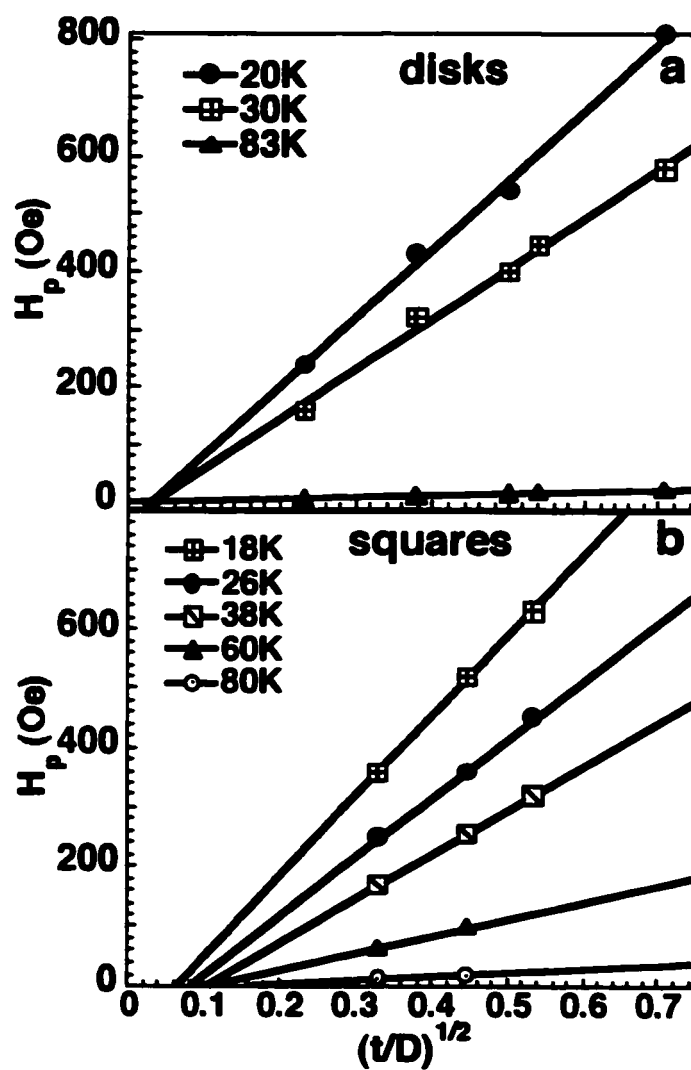
Figure 5.3: Vortex penetration field H_p vs. $\sqrt{t/D}$ for BSCCO (a) disks and (b) squares at selected temperatures.
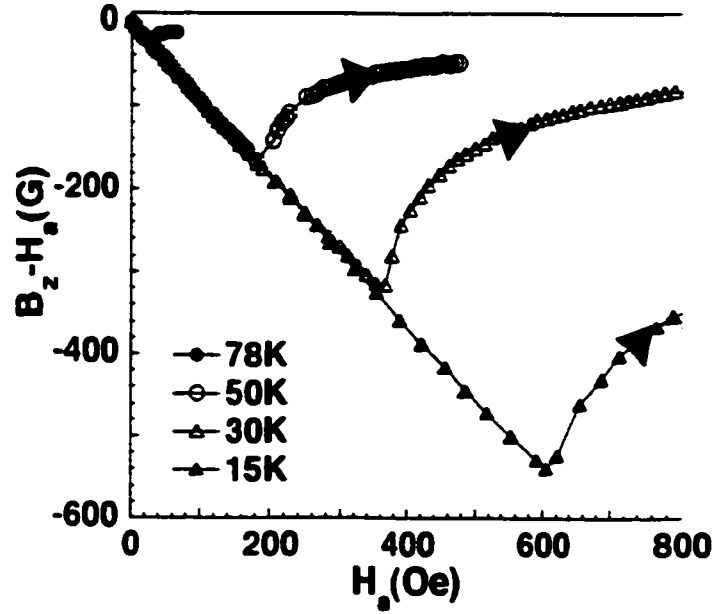
Figure 5.4: $B_z - H_a$ vs. H_a for the 50 μm BSCCO square at various temperatures.

Here D represents the diameter of a BSCCO disk and the width of a square, respectively. The solid lines are linear fits of H_p to $\sqrt{t/D}$ in units of Oe:

$$H_p = H'_{c1}(-0.2 + 7\sqrt{t/D}),$$ (5.1)

for BSCCO disks and

$$H_p = H'_{c1}(-0.6 + 7\sqrt{t/D}),$$ (5.2)

for BSCCO squares, respectively, where H'_{c1} is the adjusted lower critical field taking into account the surface barrier effects at a field ramp-rate of 1 (Oe/s) [57]. $H'_{c1} \approx 170$ Oe, 120 Oe and 5 Oe at 20 K, 30 K and 83 K, respectively [57].

Figure 5.4 shows the $B_z - H_a$ vs. H_a curves of a 50 μm BSCCO square at selected temperatures ranging from 15 K to 78 K. As temperatures increases, H_p decreases. H_p vs.
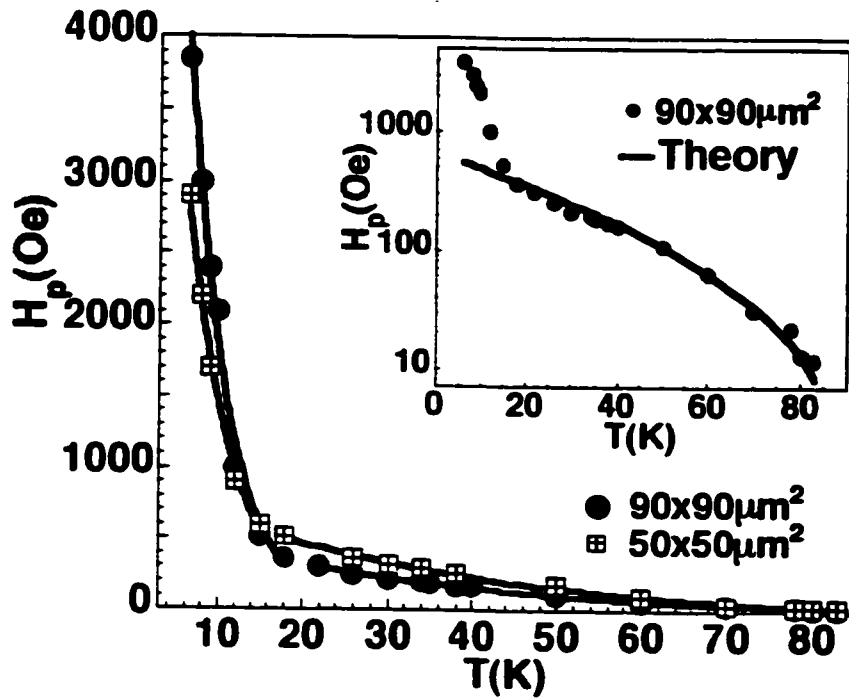
Figure 5.5: H_p vs. T for the 50 μm and 90 μm BSCCO squares. The inset compares $H_{p(SB)}$ with H_p of the 90 μm square in a logarithmic scale.

T is plotted in Fig. 5.5. H_p vs. T of a 90 μm square is also plotted for the purpose of comparison with the 50 μm square. The solid lines below 15 K in Fig. 5.5 are exponential fits of H_p as a function of temperature. The exponential fits of the 50 μm and the 90 μm squares meets at 15 K. Therefore we consider 15 K to be the transition point at which the behavior of H_p changes: $H_p(90\mu\text{m}) \geq H_p(50\mu\text{m})$ below 15 K and vice versa above 15 K; H_p increases abruptly below 15 K and is smooth above 15 K. In the following sections, we discuss separately H_p at temperatures above and below 15 K.

5.3 Analysis Using the Surface Barrier Models

Above 15 K. the bulk pinning energy barrier is negligible [58], so we consider only the surface barriers when analyzing H_p. Since the surface barriers are assumed to be functions of $\sqrt{t/D}$ [32, 34, 35, 53, 54, 58, 59], we plot, for the purpose of comparison with the surface barrier models, H_p vs. $\sqrt{t/D}$ as shown in Fig. 5.3. Brandt's geometrical barrier calculation of pin-free BSCCO disks [53] predicts

$$H_{p(GB)} = H_{c1} tanh[0.67\sqrt{t/D}].$$ \hfill (5.3)

Using the 20 μm disk at 30 K as an example, we obtain from Eq.(5.3) $H_{p(GB)} = 63$ Oe with $H_{c1} = H'_{c1} = 120$ Oe [57]. It is eight-fold smaller than our experimental value of $H_p = 522$ Oe. Comparison at other temperatures above 15 K yields similar results. On the other hand. Kuznetsov's geometrical barrier calculation for type-II superconductor disks with pinning predicts

$$H_{p(GB)} = H_{c1}\frac{\sqrt{\eta/\alpha}}{N},$$ \hfill (5.4)

where η is a dimensionless parameter, α is the width-to-thickness ratio D/t of the disk. and N is the enhancement factor [54]. Given that $\sqrt{\eta}/N$ is of order unity for our sample sizes [54], $H_{p(GB)}$ is six-fold lower than our experimental H_p. Thus, the geometrical barrier is ruled out as the dominating energy barrier at temperatures above 15 K for micron-sized BSCCO.

We now consider whether the Bean-Livingston surface barrier vortex penetration field H_p determines H_p at temperatures above 15 K. The Bean-Livingston model predicts

$$H_{p(SB)} = \sqrt{t/D}H_c(T)exp(-T/T_0),$$ \hfill (5.5)

where H_c is the thermodynamic critical field and T_0 is the characteristic temperature [34]. The magnitudes of the Bean-Livingston $H_{p(SB)}$ and our experimental H_p are comparable. We compare the temperature dependences in the inset to Fig. 5.5 for a 90 μm disk. By using $H_c \approx \kappa/ln\kappa H_{c1}$ [35], where $\kappa = \lambda/\xi$ is the ratio of the penetration depth λ and the coherence length ξ, and $H_{c1}(T) = H_{c1}(0)[1 - (T/T_c)^2]$ [17], Eq. 5.5 can be written as $H_{p(SB)}$ $= \sqrt{t/D}\kappa/ln\kappa H_{c1}(0)[1 - (T/T_c)^2]exp(-T/T_0)$. The solid line in the inset to Fig. 5.5 is the best fit of $H_{p[SB]}$ to the 90 μm square, which gives reasonable fitting parameters: $T_0 = 35$ K [34] and $\kappa/ln\kappa H_{c1}(0) \approx 2000$ Oe, knowing that $\kappa/ln\kappa$ is of order ten [35] and $H_{c1}(0) \approx 200$ Oe [58]. $H_{p(SB)}$ agree well with H_p above 15 K. Similar agreements are obtained for other sized samples. We conclude that above 15 K, H_p in micron-sized BSCCO is determined by the Bean-Livingston surface barrier effect.

Below 15 K, H_p rises sharply and is approximately proportional to the sample width D as shown in the main body of Fig. 5.5. The Bean bulk pinning model prediction of H_p is [28, 17]

$$H_{p(BP)} = 2\pi J_c D/c, \tag{5.6}$$

where the critical current $J_c(T) \approx J_c(0)exp(-T/T_1)$ [54], T_1 is the critical current temperature exponent and is of order 10 K, and c is the speed of light. The solid lines below 15 K in Fig. 5.5 are exponential fits of H_p as a function of temperature:

$$H_p \approx 186D(\mu m)exp(-T/5K)(Oe). \tag{5.7}$$

When comparing with Eq. 5.6, Eq. 5.7 gives reasonable values of $J_c(0) \approx 3 \times 10^6$ (A/cm^2) [17] and $T_1 = 5$ K. $T_1 = 5$ K is consistent with our previous result of T_1 in Ref. [27]. We consider H_p to be in reasonably good agreement with $H_{p(BP)}$ below 15 K.

We thus find that for BSCCO of our sample sizes, below 15 K, the Bean bulk pinning energy barrier determines the vortex penetration field; above 15 K, the Bean-Livingston surface barrier effect dominates (The distributed surface barrier model [60] also supports our results). For larger samples (millimeter-sized) with similar sample thickness of order 10 μm, t/D is much smaller in comparison to our micron-sized samples. Thus, at a given temperature, the dominating energy barriers in large BSCCO samples can differ from those in micron-sized samples.

Chapter 6

Josephson Vortex Locking in

BSCCO

6.1 Introduction

In the vortex liquid state of BSCCO, the triangular vortex line lattice dissociates into triangular 2-D pancake lattices in the CuO_2 planes as the magnetic field applied along the c-axis increases. When the high magnetic field tilts away from the c-axis, a triangular Josephson vortex lattice forms in between the layers. There are now pancake and Josephson vortices coexisting inside the sample [61, 62]. They influence each other through magnetic coupling [62]. To lower the sample's total free energy, the relative position of the triangular pancake lattices are adjusted to a new configuration.

Vortex pinning also plays a role in rearranging the pancakes. Pancake vortices are pinned by the random in-plane pinning centers, so they cannot move far from their

original positions. The Josephson vortices are pinned as well through their interaction with the pinned pancake vortices [63]. It is the sum of the magnetic coupling interaction and the mutual pinning interaction of the two vortices that determines the final vortex configuration. Since pinned Josephson vortices influence the c-axis critical current, this new pancake configuration can be probed using the c-axis resistance measurements. For the purpose of better understanding the pancake and Josephson vortices' interactions in tilted fields, we have studied the c-axis magneto-resistance of BSCCO single crystals in tilted magnetic fields.

We have observed that at a given magnetic field and temperature, the c-axis magneto-resistance decreases with θ, the angle between the applied magnetic fields and the ab-plane of BSCCO, until angles within one degree of the ab-plane direction. Near one degree, the resistance peaks suddenly. Similar phenomena have been observed in other c-axis magneto-resistance measurements [64, 65, 66]; however, the origin of this narrow resistance peak remains unclear. The width of the resistance peaks increases linearly with the applied field H_a in a manner that agrees with the zigzag pancake arrangement model [65]. According to the zigzag pancake arrangement model, pancake vortices arrange in a zigzag structure along the c-axis instead of stacking on top of each other and forming a straight vortex line. A c-axis critical current maximum (resistance minimum) occurs whenever the tilt angle is suitable for the formation of a zigzag pancake arrangement.

We have also found that our center peak phenomena were identical to that in ab-plane magneto-resistance measurements [2, 3, 67]. This coincidence is surprising since it is not obvious that the origins of the in- and out-of-plane magneto-resistances are the same,
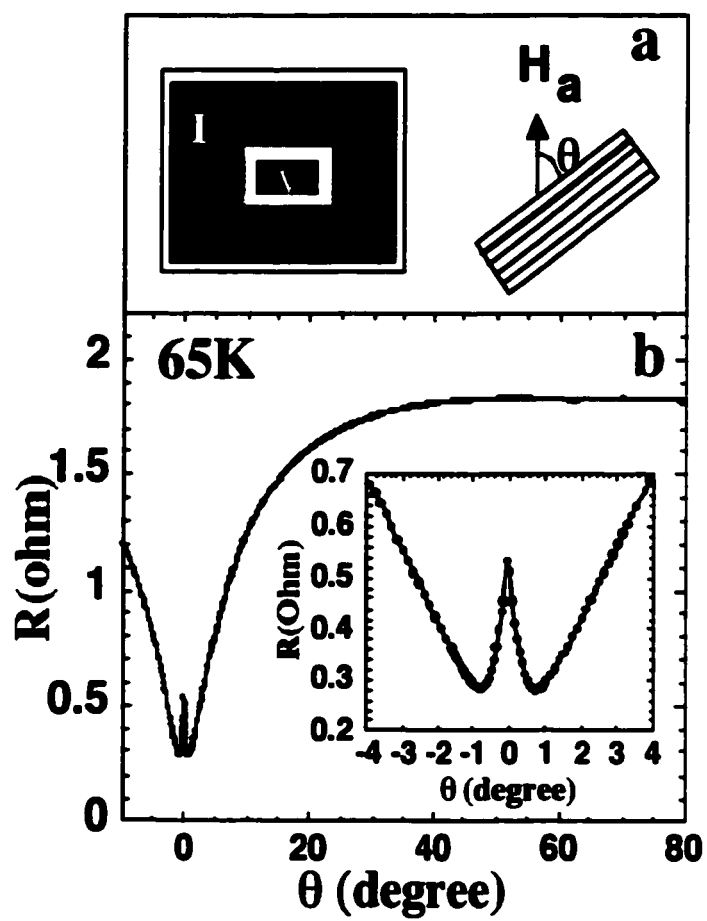
Figure 6.1: (a) Schematics of our donut-shaped four-probe contact geometry on a sample in a tilted magnetic field H_a. θ is the angle between H_a and the ab-plane direction of the sample. (b) R vs. θ curve at 65 K and 8 T. The inset emphasizes the sharp dissipation peak at $\theta = 0$.

especially in tilted fields. Koshelev has shown that the in- and out-of-plane dissipations of BSCCO have the same origin for magnetic fields parallel to the c-axis [68]. Since the experimental parameters of our peak phenomena fit Koshelev's model, we propose his calculation to be applicable to all tilt angles.

6.2 Experimental Set-Up

The sample for our measurements is $1.3\text{mm}\times1\text{mm}\times20\mu\text{m}$ in size. Four-probe silver paint contacts are patterned onto both sides of the sample. Figure 6.1(a) shows the schematics of the contact configuration. The donut-shaped current contacts cover most of the sample surfaces to ensure a homogeneous current flow across the sample layers. The voltage probes are located at the center on both sides of the sample. The sample is overdoped $(T_c = 81 \text{ K})$ by annealing in air at 450°C for 14 h. Then the sample is mounted onto a rotational stage probe that is placed in a superconducting solenoid. The angular resolution of the rotational stage is 0.01°. The angle between the applied magnetic field H_a and the ab-planes of the sample is denoted by θ as shown in Fig. 1(a).

6.3 C-axis Resistance Peaks

Figure 6.1(b) shows the resistance R vs. θ curve at 65 K and 8 T. The current density is 0.1 A/cm^2. The resistance decreases with θ continuously and drops sharply at near 20°. At angles near $\theta = 0$, the resistance peaks suddenly. The inset to Fig. 6.1(b) shows a detailed view of the peak with a width of within two degrees.

Figure 6.2 shows the center resistance peak at 70 K for H_a ranging from 1 T to
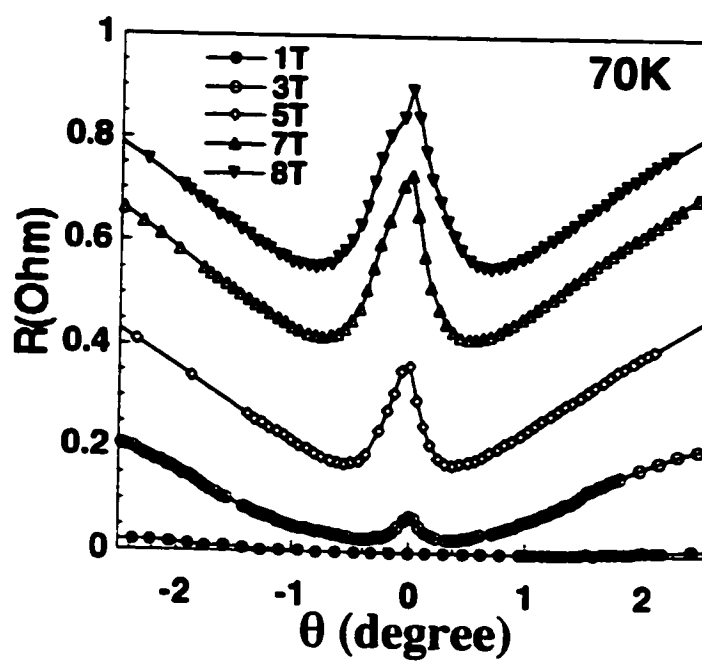
Figure 6.2: R vs. θ at 70 K. H_a ranges from 1 T-8 T. All peaks are within $1°$ to $\theta = 0$. The width of the peaks is defined as the angular difference between the two resistance dips. The width of the peaks increases linearly with H_a.
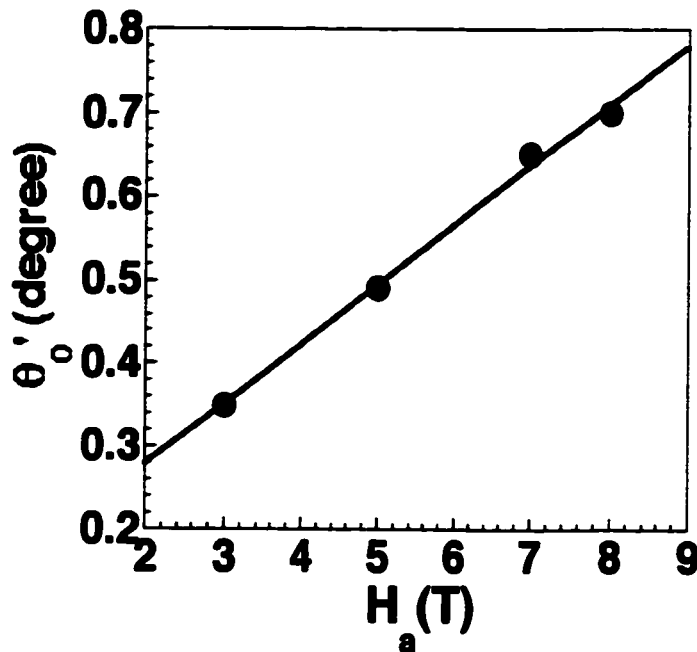
Figure 6.3: θ'_0 vs. H_a at 70 K. θ'_0 increases linearly with H_a as $\theta'_0 = -0.13 + 0.07 H_a$.

8 T. The angle difference between the two resistance dips next to $\theta = 0$ is defined as the width of the peak $\Delta\theta$. Notice that $\Delta\theta$ is $< 2°$ for all fields. $\Delta\theta$ also increases with H_a. Here we define $1/2\Delta\theta$ as θ'_0, representing the angle at which the resistance dip occurs (indicating the zigzag pancake arrangement). θ'_0 and H_a have a linear relationship at all temperatures where the center peak phenomena are observed as

$$\theta'_0 = -0.13 + 0.07 H_a. \qquad (6.1)$$

Figure 6.3 plots the linear θ'_0 vs. H_a curve at 70 K.

Figure 6.4 shows the center peaks at different temperatures at 8 T. The values of θ'_0 are identical at all temperatures. For the two temperatures of 45 K and 50 K, Fig. 6.5 shows that the center resistance patterns are different from the peak structures at higher
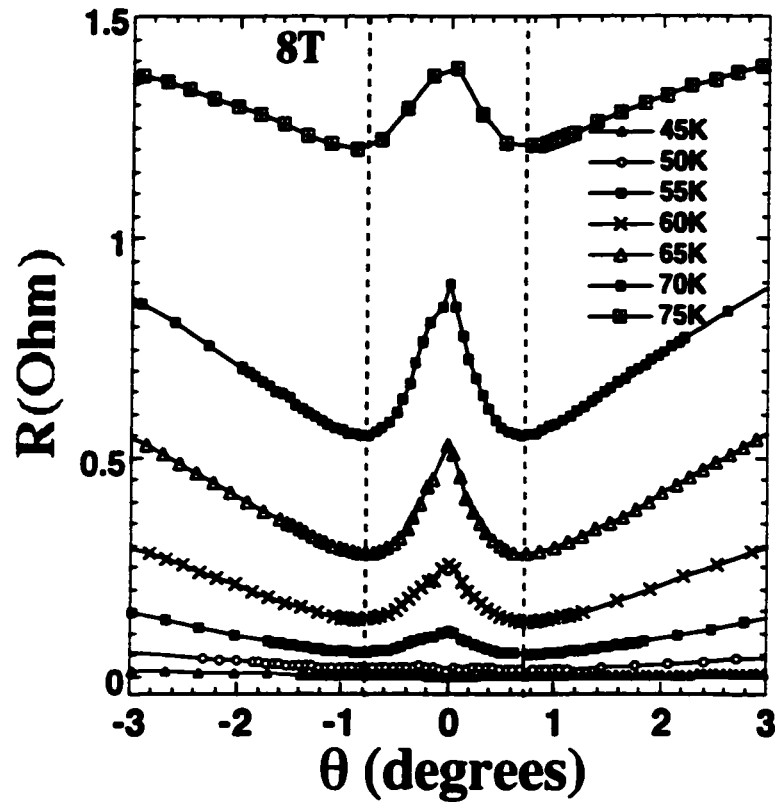
Figure 6.4: Dissipation peaks at temperatures ranging from 45 K to 75 K at 8 T. The dashed lines are guides for the eye that all peaks have the same half width of 0.8°.

temperatures. The resistance vs. θ plot show a dip at $\theta = 0$.

What is the origin of the resistance peak at $\theta = 0$? The answer lies in the interaction of pancakes and Josephson vortices at low tilt angles and high magnetic fields. When the magnetic field tilts away from the c-axis of a BSCCO sample, H_a can be discomposed into an $H_{a\parallel}$ component parallel to the ab-planes and an $H_{a\perp}$ component parallel to the c-axis of the crystal, respectively. The in-plane component of the field $H_{a\parallel}$ creates a Josephson vortex lattice in between the layers. When the c-axis component of the field $H_{a\perp}$ reaches the ab-plane vortex penetration field $H_{c1}(1 - N)$ (H_{c1} is the lower critical field
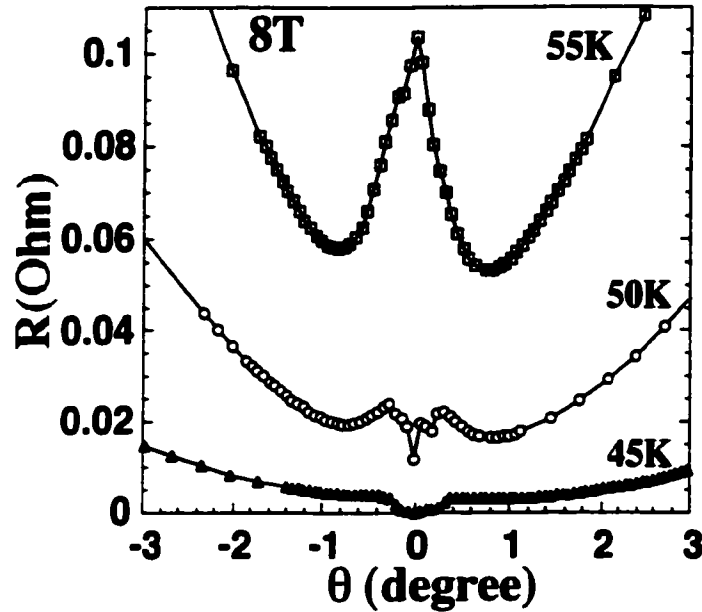
Figure 6.5: A detailed view of the resistance peak and dips at 55 K, 50 K and 45 K and 8 T. Notice that the resistances dip at $\theta = 0$ for the 50 K and 45 K data.

and N is the demagnetization factor), pancake vortex lattices form in the ab-planes of the sample. Both vortices have a triangular lattice structure and they coexist in the sample [62]. The c-axis dissipation has contributions from both vortices. Josephson vortices generated c-axis dissipation originates from their in-plane motion driven by a transport current. The pancakes' contribution originates from thermal fluctuations which induce phase fluctuations in the c-axis tunneling Josephson current [68]. Pancakes interact with Josephson vortices through the kinetic energy of currents in the layers and Josephson coupling [65]. Since the pancakes are pinned in the layers by random pinning centers, their interaction with Josephson vortices in turn pins the Josephson vortices as well. When the Josephson vortices are pinned, the c-axis critical current J_c increases and the out-of-plane resistance decreases. As a result, we observe resistance dips by $\theta = 0$. The dissipation peaks are observed when the
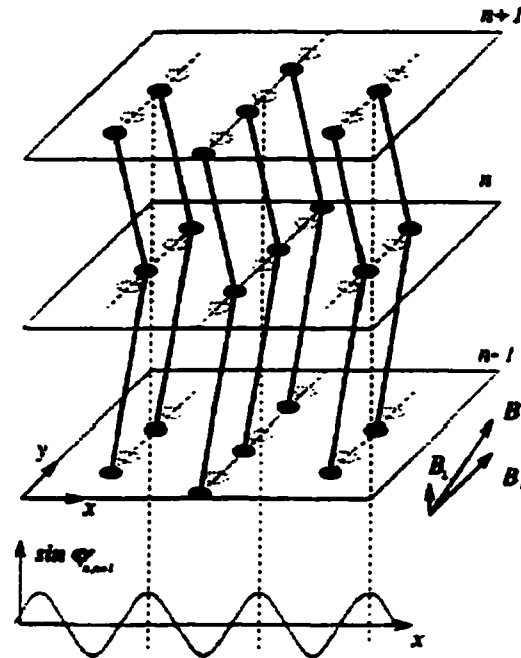
Figure 6.6: Zigzag arrangement of pancake vortices in BSCCO at low tilt angles and high fields (Bulaevskii et al.,1996).

Josephson vortices are not pinned strongly by pancake vortices, at $\theta = 0$.

6.4 Zigzag Pancake Arrangement Model

We now discuss how measurements of the width of the center peaks allow us to obtain the pancakes' new arrangements relative to the Josephson vortices. Pancake vortices enter the sample when $H_{a\perp}$ at low tilt angles exceeds the lower critical field $H_{c1}(1 - N)$ [65] (where $N \approx 0.8$ for typically plate-shaped BSCCO samples). $H_{a\parallel}$ has to exceed a critical high field limit H_0 for the magnetic field to penetrate into the layers freely and form a

Josephson vortex lattice. That is,

$$H_{a\parallel} > H_0 = \frac{\Phi_0}{\pi\gamma s^2},$$ (6.2)

where Φ_0 is the superconducting quantum flux, γ is the anisotropy ratio and $s \approx 16$ Å is the spacing between copper-oxide double layers [69]. L. N. Bulaevskii et al. have calculated the pancake and Josephson vortices interaction within these high field and low tilt angle limits and predicted that the pancakes arrange in a zigzag configuration along the c-axis to lower the total free energy of the sample. The vector jointing the nearest neighbors of the ab-plane pancake vortex lattice points along the Josephson vortex direction. This pancake arrangement occurs whenever the lateral pancake lattice spacing matches that of the Josephson vortex at a proper tilt angle. Figure 6.6 shows this zigzag pancake arrangement in alignment with the underlying Josephson vortices. The Josephson vortex pinning maximum (resistance dip) occur whenever there is a matching of the vortex lattice spacing. The first matching angle for the zigzag pancake arrangement is shown to be [65]

$$\theta_0 = \frac{s^2 B\sqrt{3}}{2\Phi_0} = 0.061B,$$ (6.3)

here B stands for the applied field H_a.

To compare our measurements with the zigzag pancake arrangement model, we need to verify that our experimental parameters match that of the model. Both components of our magnetic fields are within the range of the model. We observe center dissipation peaks only at fields above 1 T ($H_{a\parallel} \approx 1$ T). This cutoff c-axis field of 1 T meets the high-field limit of the model of $H_{a\parallel} > H_0 \approx 1$ T using $\gamma \approx 200$. Our $H_{a\perp}$ at fields above 1 T exceeds the lower critical field $H_{c1}(1 - N)$ required for pancakes to enter the sample. At 1 T and the first

zigzag configuration onset angle of $\theta_0 = 0.8°$, $H_{a\perp} = 1(T)\sin(0.8°) = 140$ Oe, higher than $H_{c1}(1 - N)$ of order 100 Oe for temperatures above 45 K [57].

Now we can compare our data to the zigzag pancake arrangement model. Equation 6.3 for the first pancake onset angle is compared to our first resistance dip angle θ'_0. Our observed $\theta'_0 = 0.13 + 0.072H_a$ agrees nicely with $\theta_0 = 0.061H_a$ in Eq. 6.1. In addition, agreeable with θ_0, we have shown that θ'_0 was temperature independent.

The zigzag pancake model predicts an additional lattice matching resonance at lower matching angles

$$\theta_m = \frac{\theta_0}{m^2},\tag{6.4}$$

where m is an integer. Additional dissipation dips should appear at θ_ms with $m > 1$. At 8 T, the second resonance ($m = 2$) should appear at $\theta_2 = \frac{\theta_0}{2^2} = \frac{0.8°}{4} = 0.2°$. θ_2 at 8 T matches our second dissipation dip at $0.2°$ in the 50 K data (Fig. 6.5). The small shoulder at $-0.2°$ in the 55 K data and the center resistance dip in the 45 K data are all signatures of this second resonance. For our experiments, the second resonance resistance dip at θ_2 is only observed at high field and low temperatures (8 T, T< 50 K). These are reasonable because the center peak height increases with the field, and the resistance dip decreases with temperature (due to stronger pancake and Josephson vortex pinning at low temperatures [70]), so only at high fields and low temperatures can the resistance contrast between the peak and the dip be large enough for us to observe.

The center resistance peaks are observed only at temperatures above 50 K, this range of temperature agrees with our value of the current density. The center dissipation peaks are current density dependent. When the applied current J is higher than the c-axis

critical current J_c, the higher the current, the higher the center resistance peak and the c-axis dissipation is proportional to $(J - J_c)$[4]. When J is lower than J_c, less dissipation should be observed at $\theta = 0$. At 50 K, the lower temperature boundary for the center dissipation peaks, our current density $J = 0.1$ A/cm^2 is higher than J_c of order 0.01 A/cm^2 (at 7.5 T) [70]. Below 50 K, J_c increases by ten-fold within 10 K and our current density becomes lower than J_c. Therefore, we do not observe dissipation peaks. Instead, we observe dissipation dips at $\theta = 0$.

6.5 Identical Origin for In- and Out-of-Plane Dissipations

We have observed another puzzling phenomena when comparing our c-axis measurements to similar ab-plane magneto-resistance measurements in tilted fields [2, 67, 3]. The ab-plane R vs. θ measurements show identical center peak structures as our c-axis measurements. Figures 6.7(a) and 6.7(b) show the ab-plane R vs. θ measurements in BSCCO taken from Refs. [2] and [3], respectively. Figure 6.7(a) shows the center peak structures of a BSCCO single crystal measured at 4 T and 50 K. Identical to our results, all center features are within 1° to $\theta = 0$. The peak height increases with the current density, like the c-axis resistance measurements in Refs. [65] and [66]. Figure 6.7(b) shows the R vs. θ curves of a BSCCO film at different temperatures at 5 T. Center dip structures appear at low temperatures, just like our data in Fig. 6.5. We thus speculate that the in- and out-of-plane dissipations have the same origin in BSCCO in tilted fields.

For magnetic fields parallel to the c-axis of BSCCO, Koshelev has shown that the in- and out-of-plane magneto-resistances are caused by the same fluctuating pancake
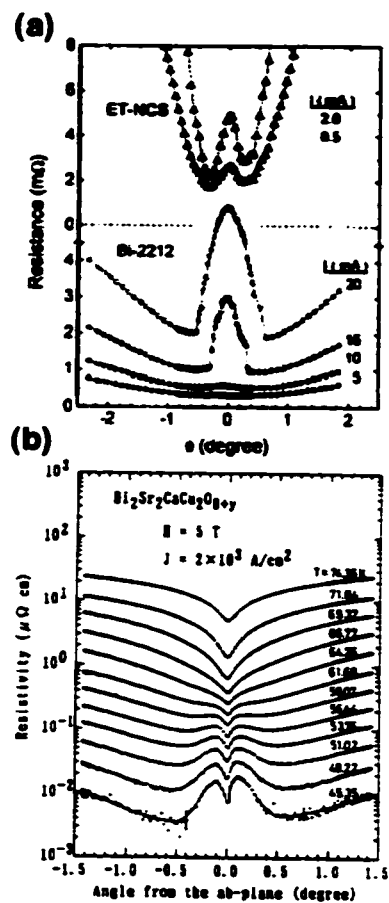
Figure 6.7: (a) R vs. θ in a BSCCO single crystal at various applied current densities. The data are taken from Ref. [2]. The applied field is 4 T and the temperature is 50 K. Notice that the peak width and height increase with the current density. (b) R vs. θ in BSCCO films at 5 T and at temperatures ranging from 45.35 K to 74.36 K. The data are taken from Ref. [3]. Similar to our result, the center resistance dip structures appear at low temperatures.

vortices [68]. As a result, the c-axis and ab-plane conductivities are proportional to each other as [68]

$$\sigma_c \approx C \frac{\Phi_0 s^2 E_j^2}{B T^2} \sigma_{ab},$$ (6.5)

where E_j is the electric field induced by pancakes' motion, B is the magnetic field and $C = 2\pi/ln(nr^2_{max})ln(r_{max}/a_0)$, with n being the pancake vortex concentration, r_{max} the cutoff phase coherence distance and a_0 the average inter-vortex spacing. Our experiments differ from Koshelev's model in that our peak phenomena are observed in tilted fields. We speculate that Koshelev's calculation can be applied to tilted angles for the following reasons: First, our σ_c and the σ_{ab} shown in Fig. 6.7 also have a linear relationship according to their identical center peak features. Secondly, according to Koshelev's calculation, the $\frac{\sigma_c}{\sigma_{ab}}$ ratio depends only on magnetic field, temperature, and sample parameters, it is independent of the exact mechanisms that cause the dissipation. So even if the dissipation mechanisms in tilted fields differ from that of fields parallel to the c-axis, the $\frac{\sigma_c}{\sigma_{ab}}$ ratio could still stand. Finally, Eq. 6.5 is valid at the temperatures range of 50 K and 70 K, this agrees with the temperature range where the peaks are observed. We thus believe that the in- and out-of-plane dissipations have the same origin at low tilt angles, possibly due to fluctuating Josephson vortices.

Chapter 7

Study of Bulk Vortex Matter using Corbino Disk Contacts

7.1 Background for Using Corbino Disk Contacts

A Corbino disk is a contact pattern for transport measurements that confines transport current within a disk structure. Since the conventional four-probe contact pattern has been shown to be vulnerable to the Bean-Livingston (BL) surface barrier effect [30], Corbino disk contact geometry has been widely used in BSCCO to probe bulk vortex properties [71, 72, 73, 74]. According to vortex measurements of strip-shaped samples using the four-probe contact geometry, the vortices flow across the sample driven by a transport current. The BL surface barrier effect acts against the vortices' entry into and exit from the sample at its edges. As a result, a higher proportion of the transport current flows on the sample edges to overcome the BL surface barrier. This uneven current flow pattern in
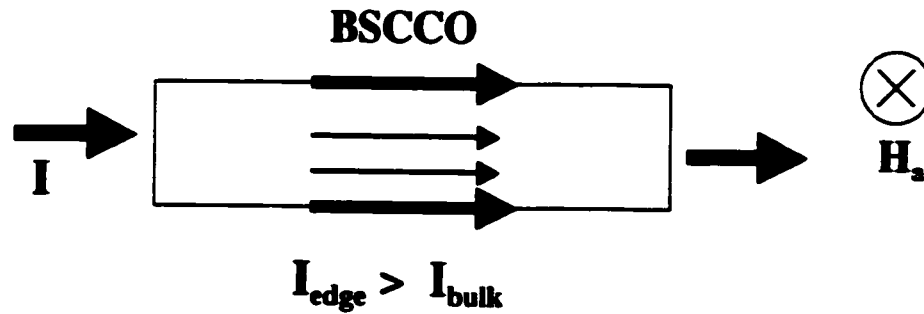
Figure 7.1: Transport current mainly flows on the surfaces of a sample due to the Bean-Livingston surface barrier effect.

a strip-shaped sample is shown in Fig. 7.1. Consequently, vortex properties probed using the conventional four-probe contact geometry are mainly edge vortex properties. Yet in a Corbino disk geometry, current and vortices are confined inside the disk. Since vortices never cross the sample edges, the BL surface barrier effect is avoided.

Although there have been many studies on vortex matter in BSCCO using a Corbino disk contact geometry, it still remains a controversy whether it is the BL surface barrier effect or the sample bulk properties that determine its vortex transport properties [72, 73]. To resolve this issue, we have performed sensitive transport measurements to probe the vortex lattice melting transition and vortex solid dissipation using a Corbino disk contact geometry. We have also designed a "Corbino disk flux-transformer" contact geometry to study the c-axis vortex correlation, avoiding the BL surface barrier effect [75, 76, 77]. All our findings via the Corbino disk method are identical to those found using the conventional four-probe geometry where the vortex properties were claimed to be determined by the BL surface barrier effect [30]. We therefore conclude that sample bulk properties determine the vortex transport properties in BSCCO.
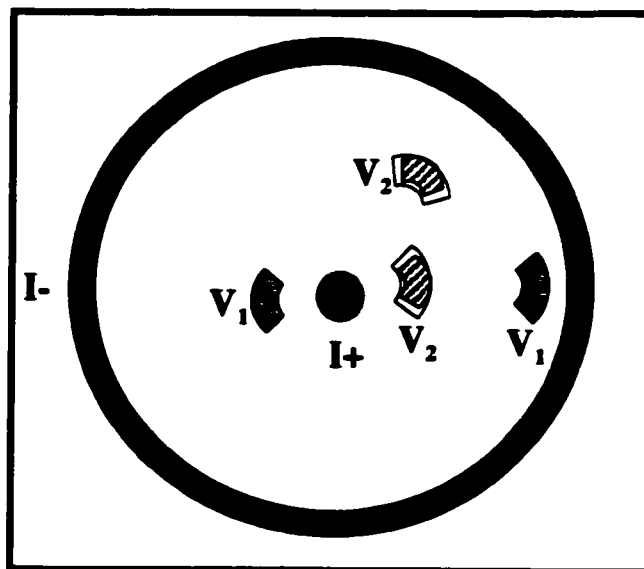
Figure 7.2: Schematics of lithographically patterned Corbino disk contacts on BSCCO.

7.2 Experimental Set-Up

The sample measured in this experiment has a dimension of $1.2\text{mm} \times 1.3\text{mm} \times 20\mu\text{m}$. Gold Corbino disk contacts are fabricated onto the sample using photolithography techniques. Figure 7.2 shows the schematics of the contacts. The outer disk has a diameter of 1 mm. Current goes in from the center and comes out of the outer ring. Since vortices move perpendicular to currents, they circulate inside the disk and never cross the sample edges. V_1 is a pair of surface contacts and V_2 is a pair of "hole" contacts at 3 μm below the sample surface. The shaded areas of V_2 contacts are the actual gold contacts and the outer boxes are the edges of the etched holes. Since the design of V_2 contacts is unconventional, we explain below in detail the design and fabrication of our "Corbino disk flux-transformer" contacts.

Flux-transformer contact geometry is mainly used in high T_c materials for transport measurements of c-axis vortex correlation. It usually contains two current contacts on the top of a sample, and two voltage contacts on the bottom. In order to study c-axis vortex correlation in BSCCO while avoiding the BL surface barrier effect, we need to put a set of flux-transformer contacts inside a Corbino disk contact. In this case, the outer disk and the center dot are the current contacts, and we need to place two voltage contacts within the disk on the bottom side of the sample. However, because BSCCO is not a transparent material, alignment of the back voltage contacts to within the top Corbino disk is nearly impossible. We in turn designed a new method to fit a pair of flux-transformer voltage contacts into a Corbino disk. We first etched holes first in the sample using the Ar^+-ionmilling technique described in a previous publication at a depth of 3 μm [37]. Then gold V_2 contacts were deposited into the etched holes (V_1 contacts and the Corbino disk pattern are also deposited at the same time). For our Corbino disk flux-transformer geometry, V_1 contacts measure the vortex dissipation R_1 at the sample surface and V_2 contacts measure the vortex dissipation R_2 at the BSCCO layer 3 μm below the sample surface. Comparison of R_1 and R_2 provides information on vortex correlation along the c-axis avoiding the BL surface barrier effect.

After the gold contacts are deposited, the BSCCO sample is then slightly overdoped ($T_c = 87$ K) by annealing in air at 550°C for 20 hours. This annealing process also helps us achieved low contact resistances of less than 0.5Ω per contact pair. It is this exceptionally low contact resistance that later enables us to measure the low vortex solid dissipation with such high precision. The sample is then placed in a superconducting solenoid with magnetic fields applied parallel to the c-axis of the sample. The resistance is measured using a 16 Hz
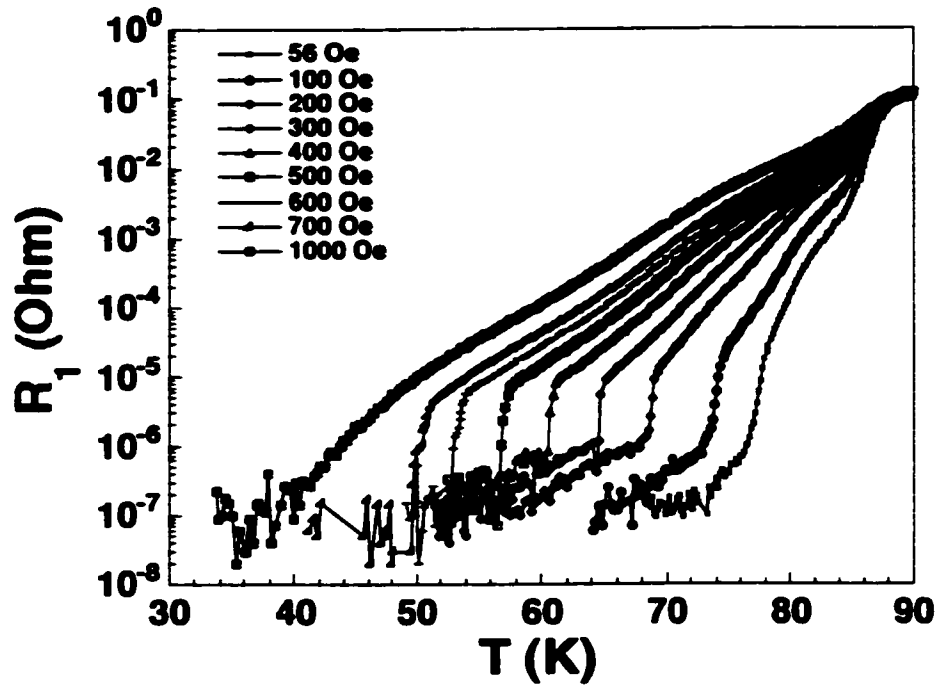
Figure 7.3: R_1 vs. T curves at magnetic fields ranging from 56 Oe to 1000 Oe. The sharp kinks represent the vortex lattice melting transition. Notice the decreasing resistances in the vortex solid state below T_m.

Ac Resistance Bridge (Model LR-700) at a current density of 10 mA.

In the following sections, we discuss R_1 and R_2 independently before comparing them in the end. All our Corbino disk results are compared to similar measurements using the conventional four-probe contact geometry. Because Corbino disk contact geometry totally avoids the BL surface barrier effect, when a result is found to be the same as that measured using the four-probe contact geometry, it can be inferred that this vortex behavior is determined by the sample bulk properties.
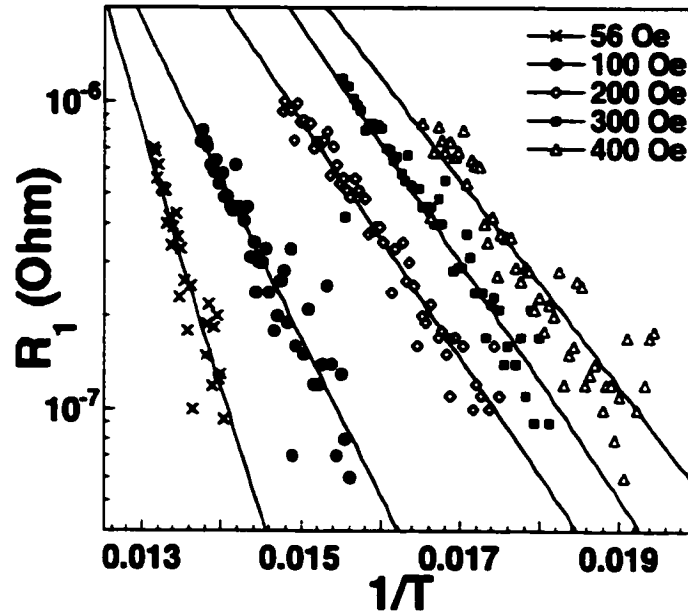
Figure 7.4: Arrhenius plots of R_1 at magnetic fields of 56 Oe, 100 Oe, 200 Oe, 300 Oe and 400 Oe. The solid lines are the best fits to the data.

7.3 Bulk Vortex Melting and Vortex Solid Dissipation

We first discuss the surface R_1 vortex dissipation patterns. Figure 7.3 shows the resistance R_1 vs. temperature curves at magnetic fields ranging from 56 Oe to 1000 Oe. At all fields, the resistance decreases with temperature and drops sharply at the vortex melting temperature T_m seen at the kinks. These kinks at T_m are signatures of the vortex lattice melting transition. The kinks begin to smear at around 1000 Oe, indicating that the melting transition is approaching the critical end-point. Our melting phase transition line and critical end-point agree with that measured in BSCCO using the four-probe contacts and other measurement methods [1, 18].

Below T_m, we enter the vortex solid phase. The vortex solid resistance can be clearly probed as shown in Fig. 7.3. These vortex solid dissipations are measured with the

highest precision among similar measurements [72, 73]. Figure 7.4 plots the vortex solid resistance in the Arrhenius form, R_1 vs. $1/T$, for various applied fields H_a. The solid lines are the best fits to data in the Arrhenius form

$$\rho = \rho_0 exp(\frac{-U_0}{T}),$$ (7.1)

where ρ_0 is the resistivity coefficient and U_0 is the activation energy of the thermally activated flux flow (TAFF). (The resistivity coefficient ρ_0 is also a function of temperature and magnetic field. However, at our vortex solid phase where $T < 0.5T_c$, the temperature dependence of ρ_0 is almost constant [78]. Therefore we may only concern ourselves with ρ_0 dependence on the magnetic field.) U_0 is a function of H_a as

$$U_0 \propto H_a^{-\alpha},$$ (7.2)

where α is a coefficient. Here we compare our U_0 obtained using a Corbino disk contact with U_0 obtained using the four-probe contacts.

The activation energies for different magnetic fields are extracted from the Arrhenius fittings in Fig. 7.4 and plotted in Fig. 7.5. The solid line is the best fit to data as

$$U_0(K) = 10850H_a^{-0.46}.$$ (7.3)

Here 0.46 is the value for α in Eq. 7.2. This value of α is equivalent to $\alpha \approx 1/2$ measured using the conventional four-probe contacts in BSCCO [78] (the magnetic field dependent magnitude of U_0 is equivalent to that measured in Ref. [72]). Therefore the vortex solid activation energy U_0 is the same for both contact geometries, and is determined by the
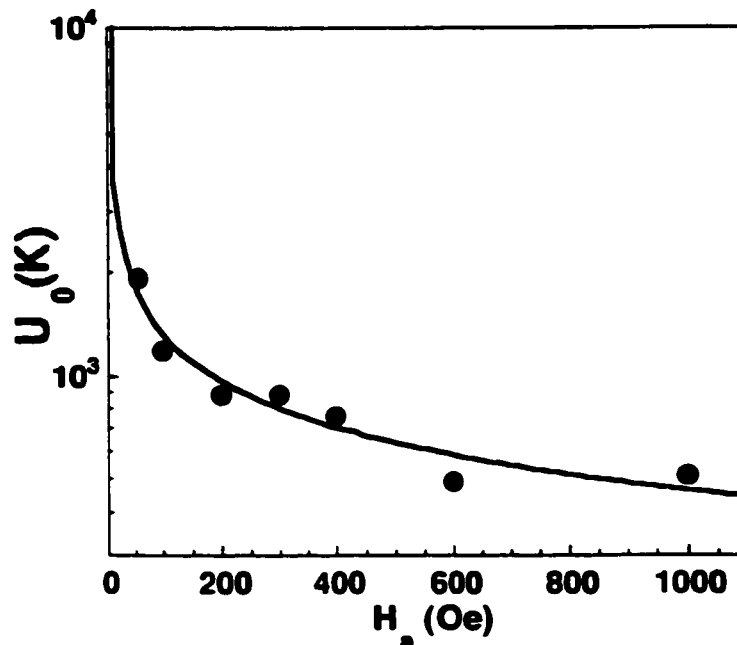
Figure 7.5: Activation energy $U_0(\mathrm{K})$ vs. the applied field H_a curve.

sample bulk properties. We thus conclude that the surface vortex dissipations (vortex liquid and vortex solid dissipations) are determined by the sample bulk properties.

7.4 Corbino Disk Flux-transformer in BSCCO

We now discuss the hole R_2 pancake resistance patterns. R_2 vs. T curves are plotted in Fig. 7.6 for H_a ranging from 0 Oe to 400 Oe. At all fields, the resistance drops rapidly to the noise level of our measurement ($10^{-7}\Omega$ at 10 mA) at T_c. At lower temperatures, the resistance rises again and reaches a plateau before it drops again at T_m. We interpret this resistance plateau as an incomplete sublimation of the 3D vortex solid to 2D pancakes [79, 80]. That is, the pancakes at deeper layers of the sample are still partially
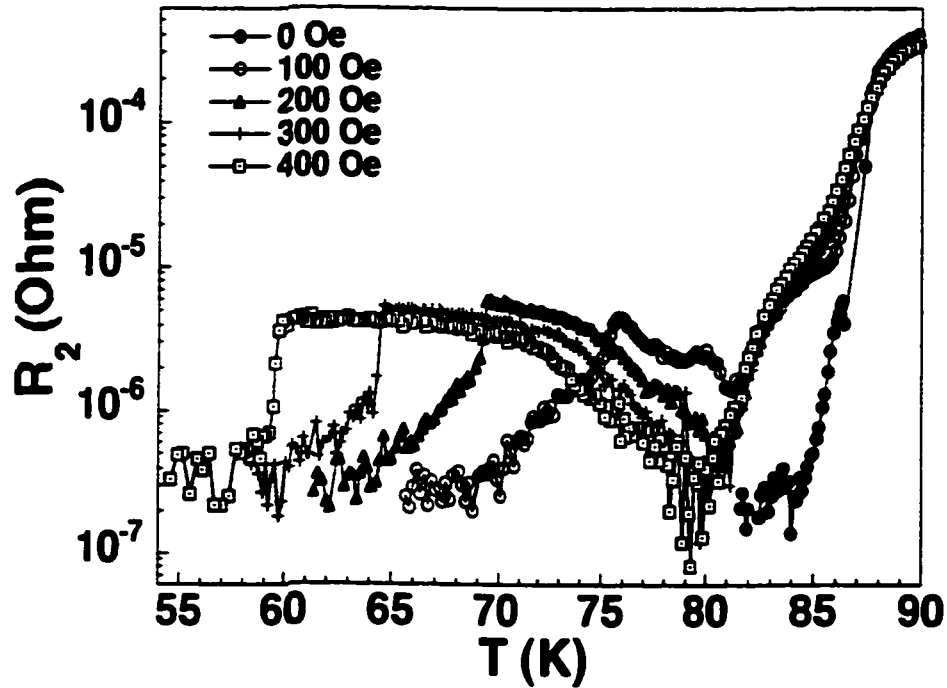
Figure 7.6: R_2 vs. T at various fields. The resistance drops to the noise level at T_c and then gradually increases at lower temperatures. R_2 drops sharply again at T_m.

correlated to the surface pancakes. If this were not true, when a vortex line dissociates completely into 2D pancakes, only the top layer pancakes would be mobile and the pancakes at 3 μm below the sample surface ($\approx$ 2000 layers of pancakes using the interlayer spacing of 16 Å) would be insensitive to the surface transport current. We believe that the vortex sublimation process completes at the resistance valley below T_c where R_2 is at the noise level. Our Corbino disk flux-transformer measurements as shown in Fig. 7.6 are identical to that measured using the conventional flux-transformer contact geometry [75, 76, 77].
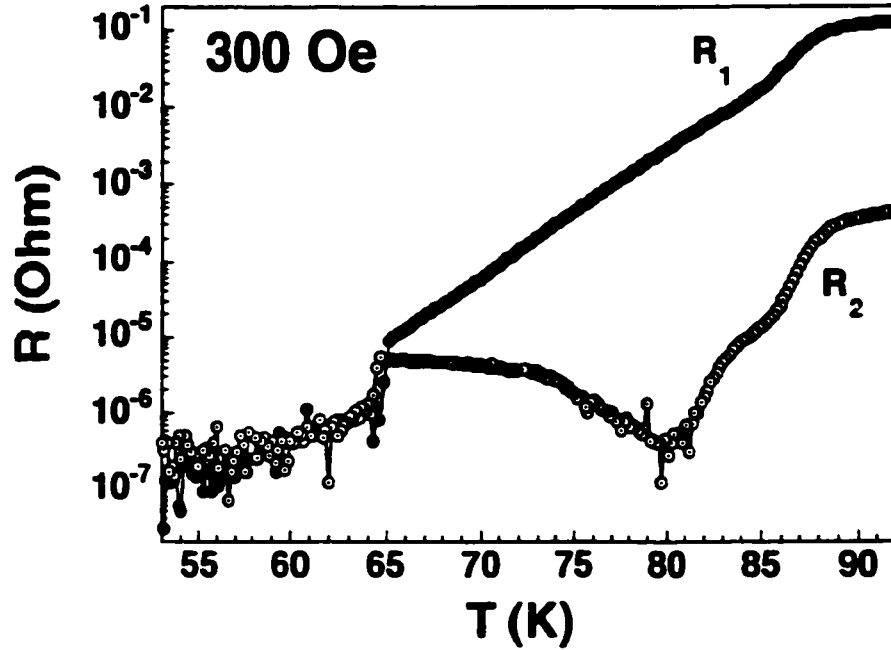
Figure 7.7: Comparison of R_1 and R_2 at 300 Oe. Their melting transitions and vortex solid resistances coincide.

7.5 C-axis Correlation of Bulk Vortex

Finally, we compare the surface and hole resistances in Fig. 7.7 at 300 Oe. Their

melting transitions occur simultaneously and vortex solid resistances coincide. R_1/R_2 is of

order 10^3 at T_c and approximately 1 at temperatures $\leq T_m$. The resistance drop from T_c to

T_m is 10^4 for R_1 and 10^2 for R_2. These resistance ratios and resistance drops are the same

as that measured using the conventional flux-transformer contacts [77]. If the BL surface

barrier dominates the vortex liquid dissipation, the resistance ratios and resistance drops of

R_1 and R_2 should be different for the two flux-transformer contact geometries. The identical

vortex solid resistances of R_1 and R_2 also indicates that the pancakes are fully correlated

along the c-axis, for otherwise R_2 would be less than R_1. The applied current at the surface

of the sample drives the whole vortex line (at least down to 3 μm below the sample surface) circulating inside the Corbino disk. It can be inferred that the c-axis vortex correlation in BSCCO is determined by the sample bulk properties.

Through our numerous measurements of the bulk vortex dissipation using Corbino disk contacts, our results agree with those measured using the conventional four-probe contact geometry. These results cover the vortex melting transition, vortex solid dissipation and c-axis vortex correlation. From these results, it is concluded that the sample bulk properties determine the vortex transport properties in BSCCO [71], rather than the previously claimed BL surface barrier effect.

Part II

Carbon Nanotubes

Chapter 8

Controlled Deposition of Single Aligned Carbon Nanotubes

8.1 Introduction

The hexagonal arrangement of covalently bonded carbon atoms into stacks of planes is known as graphite. When a layer of graphite, known as graphene, is rolled up into a tube, this tube is called a single-walled carbon nanotube.

Carbon nanotubes (CNTs) were discovered in 1991 by Ijima [80]. The tubes are usually microns long and nanometers in diameter. Carbon nanotubes can be single walled or multi-walled, where many concentric layers of graphene nest into a shell. Figure 8.1 shows the Transmission Electron Microscope (TEM) image of a multi-walled carbon nanotube synthesized using the pyrolysis method [81]. All nanotubes used in our experiments are synthesized using this method.
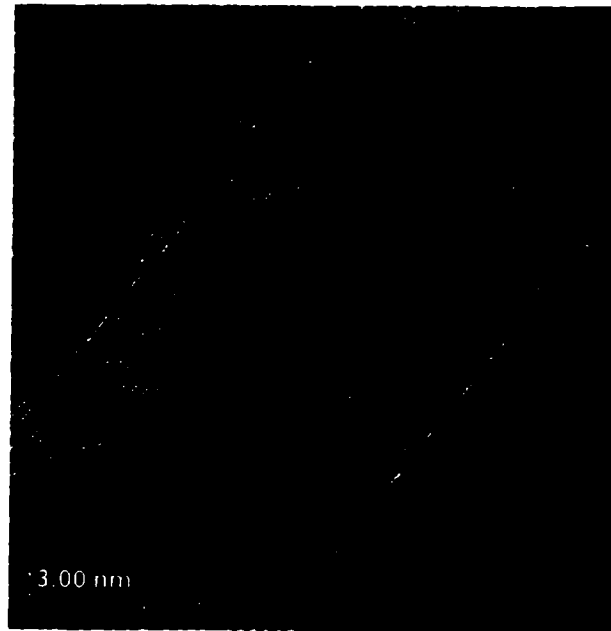
Figure 8.1: TEM image of a multi-walled carbon nanotube (courtesy of Wei-Qiang Han).

Electronically, single-walled CNTs can be metallic or semiconducting depending on their chiralities [82, 83, 84]. Semiconducting single-walled CNTs are especially desirable for application since they are the building-block material for nanotube-based transistors [85]. Mechanically, carbon nanotubes are reported to be the strongest fiber [86]; therefore, measurements of their elastic properties are important. In this chapter, we discuss the controlled deposition of multi-walled CNTs using MEMS (Microelectromechanical systems) devices. We will also discuss the bending of a single CNT *in situ* in a TEM.

8.2 Aligning Single CNTs Using Capillary Forces

Since the discovery of carbon nanotubes (CNT) in 1991 [80], CNT has been suggested to be a prominent building-block material for the next generation of nano-scale electronics. CNT-based devices include room temperature transistors [85], random access memory devices [87], p-n junctions [88] and sensitive gas sensors [89, 90]. However, the device-fabrication technique is impeded by the use of the conventional "deposit and find" method, in which nanotubes are successively deposited and then located one at a time. This laborious method cannot meet the commercialization requirement of CNT-based electronics. An innovative method to assemble single nanotubes at predetermined locations is called for.

Prior efforts on controlling the CNT depositions mainly take two approaches - synthesizing CNTs from patterned catalysts directly [91, 92] or depositing suspended CNTs onto pretreated substrates [93, 94, 95, 96, 97]. Neither approach allows complete control of the locations, the orientations, and the quantity of the nanotubes deposited.

U.S. Pat. No. 6,346,189 issued to Kong et al. discloses a method for growing single-walled carbon nanotubes from pre-patterned catalyst islands [91]. According to this method, the patterned catalysts on a substrate are heated in flowing carbon-containing gases (e.g. methane). Individual single-walled carbon nanotubes grow from the islands in all directions. Although this method is effective in fixing the locations of the nanotubes, the orientations of the nanotubes are not controlled. In addition, the number of nanotubes grown on one island is also not fixed. When one of the many nanotubes out of an island reaches another catalyst island, a functional device is formed. This method of forming random single nanotube-
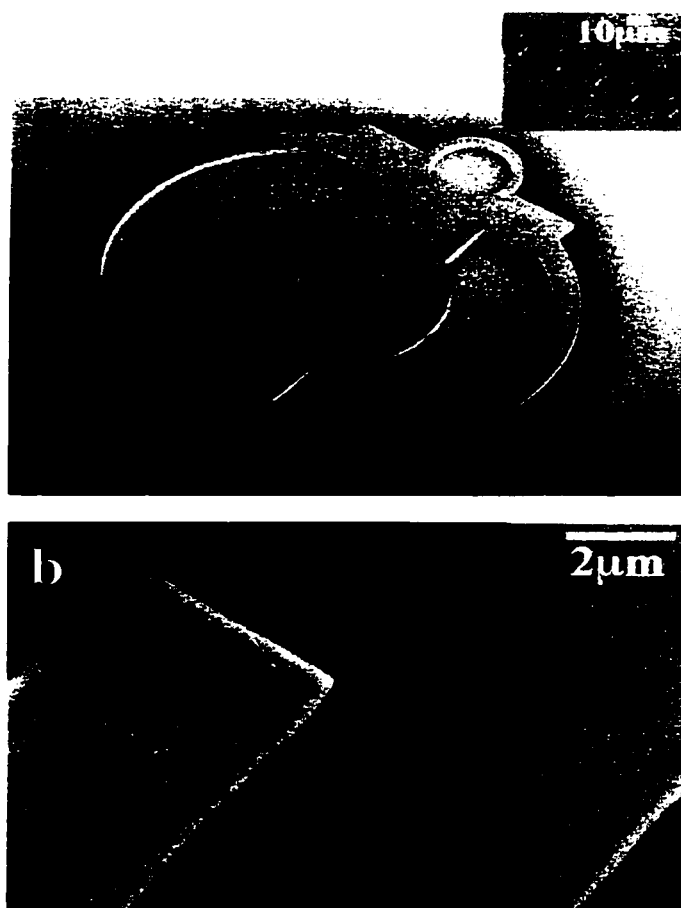
Figure 8.2: (a) SEM image of the silicon MEMS device for CNT deposition. The device is 50 μm thick. The inset is the blow up of the teeth pairs in the center of the device. (b) A straight CNT lands across a pair of contacts.
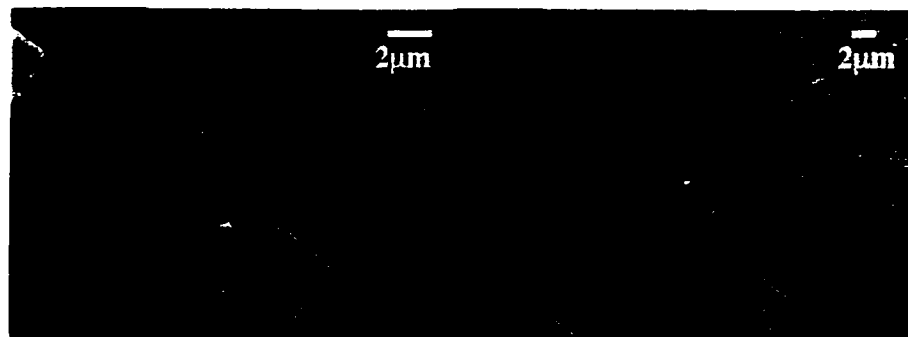
Figure 8.3: Other single nanotubes deposited on the same device as in Fig. 8.2(a).

devices by chance is insufficient for large-scale production of nanotube-based devices.

Yamamoto et al. have used the electrophoresis method to align suspended multi-walled carbon nanotubes onto a chip [94, 95, 96]. According to this method, a pair of parallel electrodes is pre-patterned onto a substrate, then a voltage drop is applied across the two electrodes and suspended nanotubes are deposited. When the solution dries, a large number of aligned nanotubes is deposited across the two electrodes. Although this method successfully positions nanotubes across the electrodes, individual nanotubes are not isolated out from the aligned nanotube bundles to form functional devices.

We have invented a simple method to deposit aligned single CNTs at predetermined locations. This method involves only a Si MEMS device, a pair of tweezers, a pipette, and a power supply. The time scale of the process is minutes. We deposit a drop of suspended CNTs onto the pre-patterned device. When the solvent (acetone) dries, 50% of the contact pairs are connected by individual CNTs. With the application of an electric field, we achieve 100% connection rates. Semiconducting nanotubes can be selectively deposited by burning off the metallic nanotubes after deposition. We consider this technique a crucial step towards
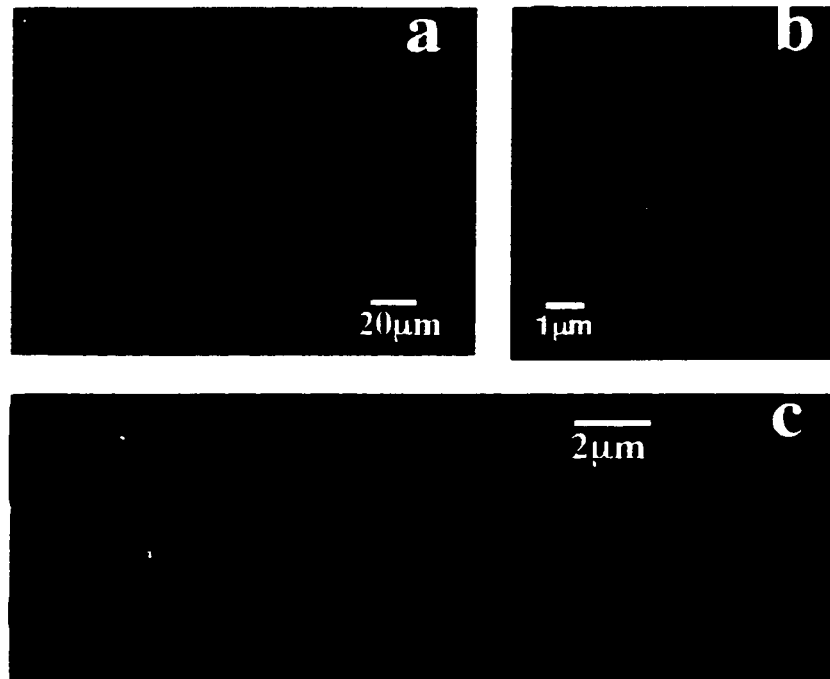
Figure 8.4: (a) Circular trenches in the center of the device. (b) A single nanotube and (c) three parallel nanotubes stretch across the trenches.

the large-scale integration of CNT-based devices.

Multi-walled CNTs are synthesized using the pyrolysis method [82]. They are suspended in acetone by sonication for 15 min. The 50 μm thick Si MEMS device [Fig. 8.2(a)] is made from a silicon-on-insulator (SOI) wafer. The teeth pairs in the center of the device [inset to Fig. 8.2(a)] are the predetermined locations for CNT deposition.

The device is held in the air by a pair of tweezers and a nanotube droplet is deposited using a glass pipette. The droplet bulges out on both sides of the device. Within one or two minutes, the droplet dries and both surfaces of the teeth pairs are connected by individual CNTs. Figure 8.2(b) shows a single carbon nanotube connecting a contact pair. The nanotube is suspended straight across without sagging. The area in the vicinity

is clean. Two other connected single nanotubes on the same device are shown in Fig. 8.3. The ratio of the number of teeth pairs connected by one or a few nanotubes to the total number of pairs on the device is defined as the successful deposition rate. For this simple "fluid drying" deposition method using teeth pair contacts, the successful deposition rate is 20% to 50%.

Alternative geometries also trap and align nanotubes. Figure 8.4(a) shows a concentric-rings geometry. For the same deposition method, nanotubes align perpendicularly across the trenches. Figures 8.4(b) and 8.4(c) show a single and three parallel CNTs stretching across the trenches.

What mechanism attracts the suspended CNTs towards the teeth pairs? We believe it is the strong capillary force generated by the narrow center trench. The width of the trench ranges from 2 μm at regions in between a teeth pair to more than 10 μm between pairs. Micron-sized gaps are narrow enough for capillary force to come into play. When a droplet is deposited, the trench sucks in the acetone from all directions. Since capillary pressure is inversely proportional to the size of an opening, the strongest force locates in between a pair of teeth. The magnitude of the force is just strong enough to grab one CNT at a time with the inflowing acetone. The nanotube makes good contacts with Si when it lands and stays intact through the rest of the drying process.

To confirm our capillary force model, we observe the acetone drying process using a microscope. The side openings of the device dry first and the acetone retrieves to the center of the device. In the center, acetone dries away from the center trench and forms droplets in the upper and lower regions of the device as denoted by the darker dots on the device (Fig.
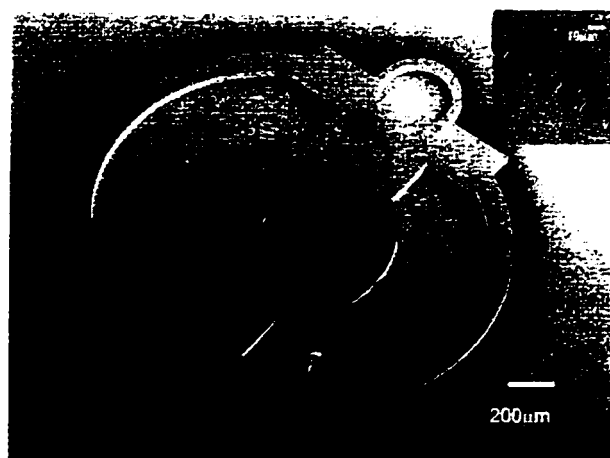
Figure 8.5: CNT droplet drying process on the device. The solvent moves away from the center gap in directions denoted by the arrows. The final droplets formed on the device are marked as darker dots.

8.5). The acetone takes unconnected nanotubes to where it dries last. This assumption is confirmed by observing nanotubes at the upper and lower centers of the device. During this time, the center trench has always been filled with acetone. Now it starts to dry. The capillary force must have been continuously drawing nearby acetone into the trench until the acetone runs out.

8.3 Electrophoresis Alignment of Single CNTs

Capillary forces trap only a fraction of the nanotubes in a droplet to the teeth pairs. To trap all nanotubes, we use electric fields. We custom design the chip so that the electric field and the electric field gradient work together to trap and align all nanotubes in a droplet. The method of using a non-uniform electric field to move a polarized dielectric particle in a dielectric medium is called dielectrophoresis. Nanotubes (semiconducting and

metallic) can be considered as point dipoles when polarize in electric fields [98]. The electric field's force on a dipole moment P is

$$F = \nabla(P \cdot E). \tag{8.1}$$

Since $P \propto E$ for dielectric particles with a linear response in electric fields, $F \propto \nabla(E \cdot E)$.

The Si device for depositions using dielectrophoresis is shown in the inset to Fig. 8.6(a). The structure consists of two Si islands separated by an array of teeth pairs. DC voltages are applied across the center trench. In a cylindrical coordinate system with the z-axis alone the trench direction, the electric field is inversely proportional to the azimuthal distance r as $E \propto 1/r$. The nanotubes can be treated as point dipoles that are always aligned with the electric field. The force $F \propto \nabla(E \cdot E)$ on a nanotube anywhere on the chip points towards the center trench. When the nanotube arrives at the trench. it strongly binds to the teeth pair contacts.

We can observe the nanotubes flying towards the center under a microscope. Figure 8.6(a) shows the aligned nanotubes at a voltage of 6 V. All teeth pairs are connected by one or a few CNTs. Excess nanotubes land on the anode side of the trench. A few nanotubes (less than 5%) are observed outside the center region. Using a higher voltage and a more dilute nanotube solution, we are able to deposit single nanotubes only. In Fig. 8.6(b). single nanotubes are aligned at 8 V with no nanotubes observed anywhere else on the chip.
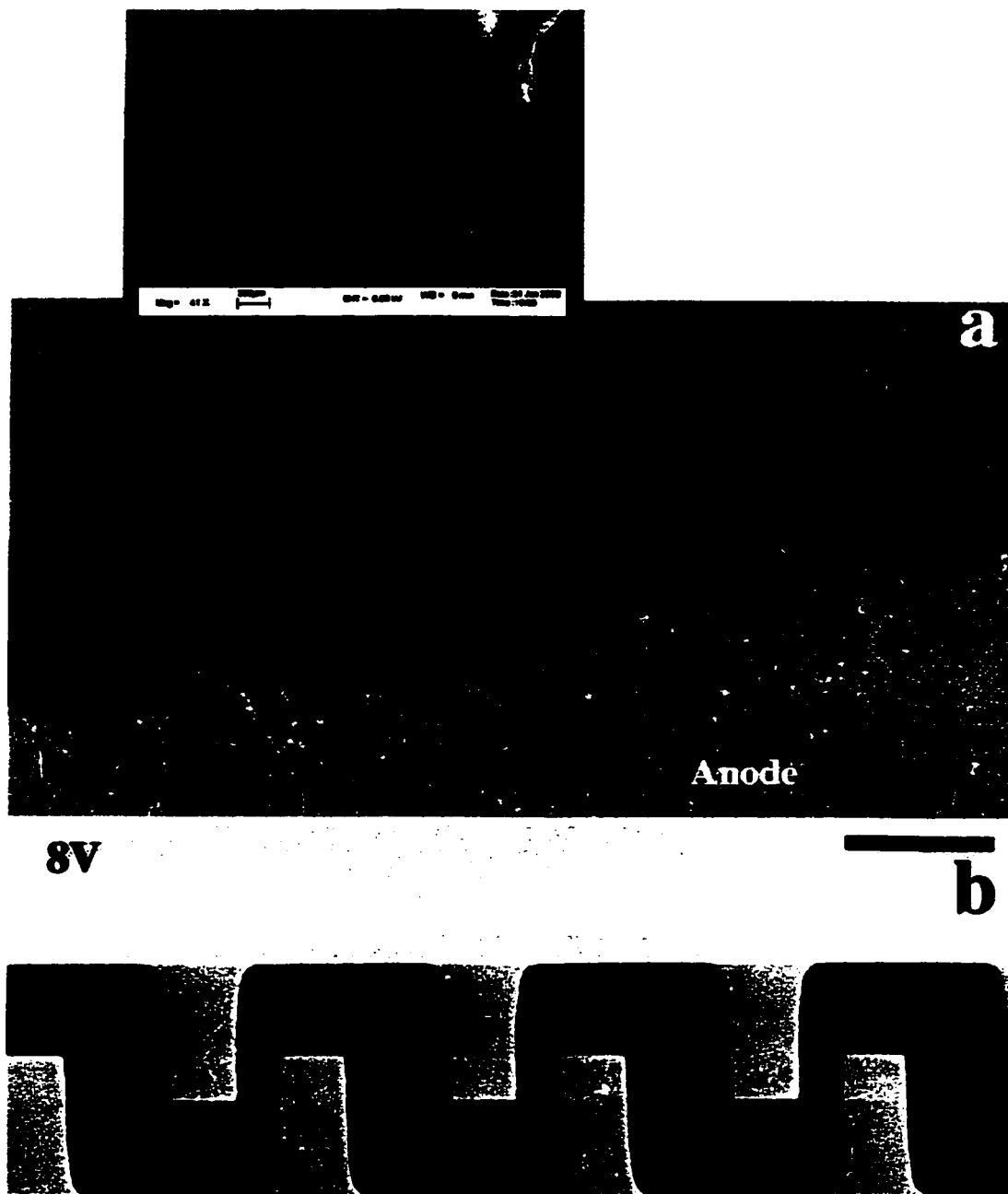
Figure 8.6: Depositions using electric fields. (a) At 6 V, all the teeth pairs are connected by single or a few nanotubes. Excess nanotubes land on the anode. (b) At a higher voltage of 8 V and a lower nanotube concentration, teeth pairs are connected by single CNTs.
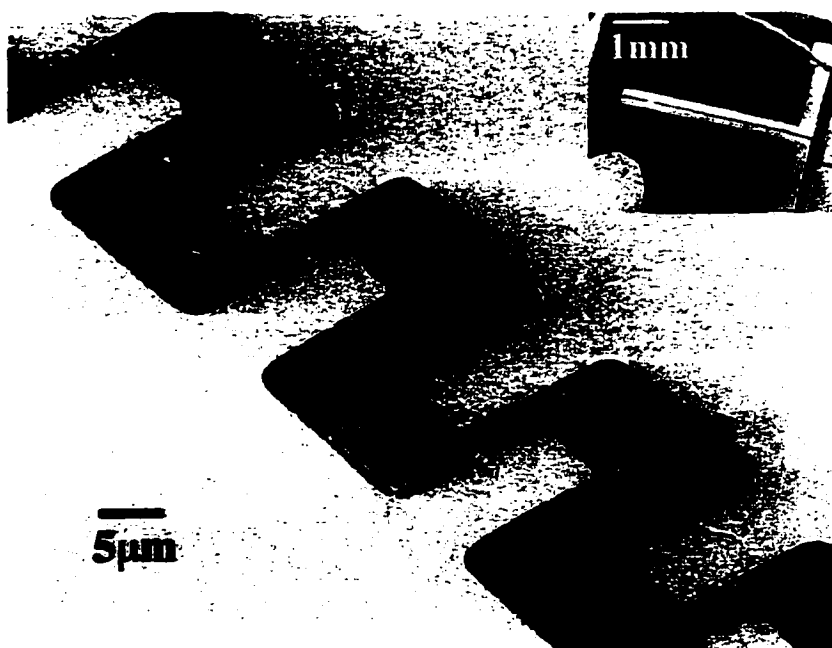
Figure 8.7: Trapping CNTs using gold electrodes at 10 V. All the nanotubes in the droplet are trapped within the center gap aligning with the electric field lines.

8.4 Nanotube Traps

We have also studied "gold" teeth patterns on oxides (inset to Fig. 8.7. At 10 V, all nanotubes are trapped within the gap along the electric field line directions. No nanotube are observed outside. We call this technique nanotube trapping. Since CNTs can be metallic and semiconducting, this technique apparently is effective in trapping both types of nanotube. However, we speculate that only semiconducting CNTs are connected for the following reason: There are 200 teeth pairs on the device and the resistance of this nanotube-connected gold device is 57 KΩ. If we assume that each contact pair in the device is connected by 20 nanotubes, and half of the connected nanotubes are metallic, then the metallic nanotubes should determine the resistance of the device. Using $R_m \approx 100$ KΩ as the
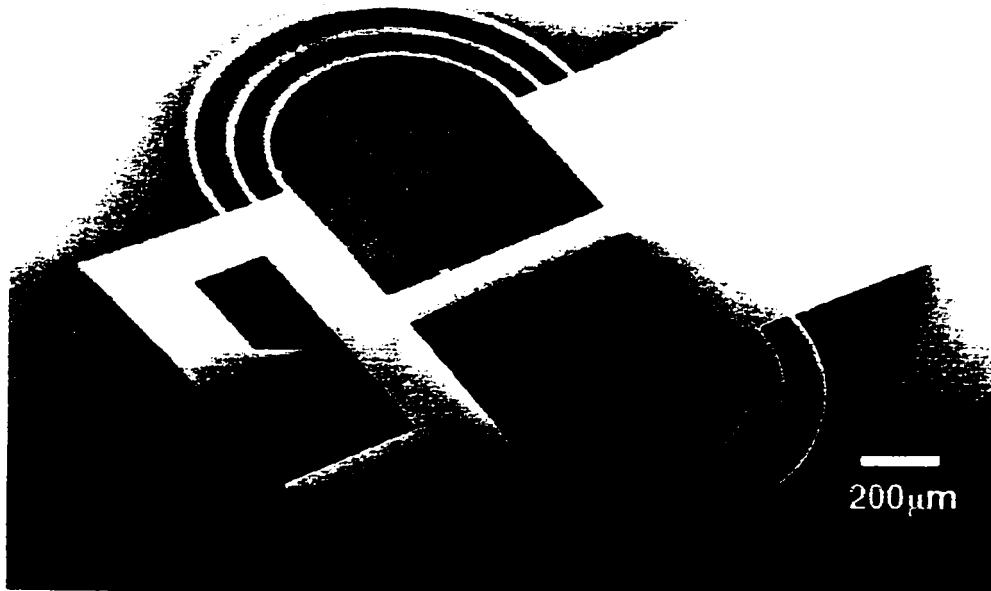
Figure 8.8: Si MEMS spring for pulling and bending of single CNTs.

two-probe resistance of a metallic CNT [99], the resistance of the device should be

$$R = \frac{R_m}{10 \times 200} = 50\Omega.$$ (8.2)

this value is 1000 times lower than our measured resistance of 57 KΩ. Could the device be connected by only semiconducting nanotubes? We calculate the current through each metallic nanotube at 10 V to be $I = 10V/(50\Omega \times 2000) = 100\ \mu\text{A}$. This current is high enough to burn up metallic nanotubes within one second [100]. Therefore, the logical explanation and conclusion are that only semiconducting nanotubes are left connected.

Figure 8.9: Center gap in the Si spring.

8.5 Bending of a Single CNT

The Si device for CNT deposition in Fig. 8.2(a) can be modified into a MEMS spring device as shown in Fig. 8.8. A 2 μm wide gap (Fig. 8.9) is etched in the middle of the center strip of the device. The spring-like nature stems from the thin and long outer rings of this device. This enables it to be elastically pulled and compressed up to a few hundred microns. It is designed to have the same size as a TEM sample grid for studying single CNTs *in situ* in TEM. In experiments, this spring device functions as a sample holder as well as a manipulator for the deposited single CNT.

Single nanotubes are deposited across the center gap of the spring (Fig. 8.9) using the "fluid drying" deposition method as described in previous sections. Figures 8.10 and 8.11 show the connected single nanotubes. The device is connected to a manipulator that contains a piece of Piezoelectric material. Figure 8.12 shows the schematics of the set-up. The Piezoelectric material retrieves or extends with the variation of an applied voltage. and therefore it pulls and pushes the spring device. The deposited single CNT on the device is thus pulled and pushed *in situ* in TEM.

Figure 8.13 shows the successive bending of a multi-walled carbon nanotube. We can see that the multi-walled CNTs are very robust under stress, for they can be bent
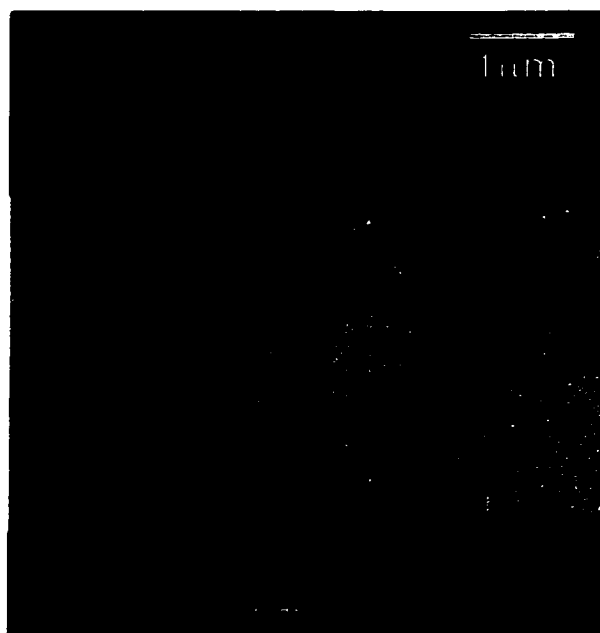
Figure 8.10: TEM image of a few carbon nanotubes deposited across the gap.

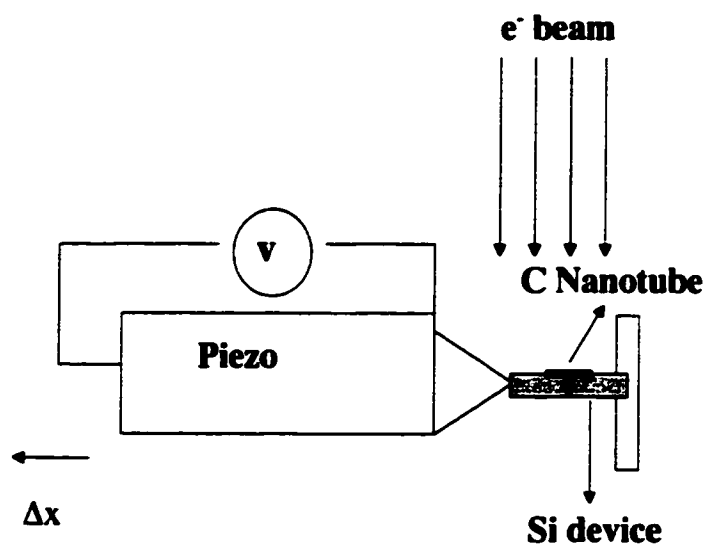Figure 8.11: One nanotube is deposited across the gap.

Figure 8.12: Schematics of the set-up for manipulating single CNTs *in situ* in TEM.

Figure 8.13: Bending of a single carbon nanotube (Wang and Demczyk).

repeatedly for more than 180 degrees with no observable damages to the tube structure.

Bibliography

[1] B. Khaykovich et al., Phys. Rev. Lett. **76**, 2555 (1996).

[2] M. Chaparala et al., Phys. Rev. B **53**, 5818 (1996).

[3] Y. Iye, T. Tamegai, and S. Nakamura, Physica C **174**, 227 (1991).

[4] J. R. Gavaler, Appl. Phys. Lett. **23**, 480 (1973).

[5] J. G. Bednorz and K. A. Müller, Z. Phys. B **64**, 189 (1986).

[6] M. K. Wu et al., Phys. Rev. Lett. **58**, 908 (1987).

[7] H. Maeda et al., Jnp. J. Appl. Phys. **27**, L209 (1988).

[8] Z. Z. Sheng and A. M. Hermann, Nature **232**, 55 (1988).

[9] C. W. Chu et al., Nature **365**, 323 (1993).

[10] T. W. Li, P. H. Kes, N. T. Hien, J. J. M. Franse, and A. A. Menovsky. J. Cryst. Growth **135**, 481 (1994).

[11] D. E. Farrell et al., Phys. Rev. Lett. **63**, 782 (1989).

[12] N. Nakamura, G. D. Gu, and N. Koshizuka, Phys. Rev. Lett. **71**, 915 (1993).

[13] A. A. Abrikosov, Soviet Phys. JEPT **5** (1957).

[14] W. H. Kleiner, L. M. Roth, and S. H. Autler, Phys. Rev. **133**, A1226 (1964).

[15] U. Essmann and H. Träuble. Phys. Lett. **24A**, 2711 (1967).

[16] W. E. Lawrence and S. Doniach, in Proc. Of the 12th International Conference on Low Temperature Physics(LT12) Kyoto 1970, edited by E. Kanda (Keigaku, Tokyo 1971) , 361.

[17] M. Tinkham, *Introduction to Superconductivity*, McGraw-Hill, New York, 1996.

[18] D. R. Nelson, Phys. Rev. Lett. **60**, 1973 (1988).

[19] D. T. Fuchs et al., Phys. Rev. B **54**, R796 (1996).

[20] R. Cubitt et al., Nature **365**, 407 (1993).

[21] A. Schilling et al., Nature **382**, 791 (1996).

[22] E. Zeldov et al., Nature **375**, 373 (1995).

[23] R. E. Hetzel, A. Sudbo, and D. A. Huse, Phys. Rev. Lett. **69**, 518 (1992).

[24] N. Avraham et al., Nature **411**, 451 (2001).

[25] M. B. Gaifullin, Y. Matsuda, N. Chikumoto, J. Shimoyama, and K. Kishio, Phys. Rev. Lett. **84**, 2945 (2000).

[26] Y. M. Wang, M. S. Fuhrer, A. Zettl, S. Ooi, and T. Tamegai. Phys. Rev. Lett. **86**. 3626 (2001).

[27] C. P. Bean, Phys. Rev. Lett. **8**, 250 (1962).

[28] E. Zeldov et al., Phys. Rev. Lett. **73**. 1428 (1994).

[29] D. T. Fuchs et al., Nature **391**, 373 (1998).

[30] M. V. Indenbom, G. D'Anna, M. O. Andre, V. V. Kabanov, and W. Benoit. Physica C **235-240**, 201 (1994).

[31] M. Benkraouda and J. Clem, Phys. Rev. B **53**, 5716 (1996).

[32] C. P. Bean and J. D. Livingston, Phys. Rev. Lett. **12**, 14 (1964).

[33] L. Burlachkov, V. B. Geshkenbein, A. E. Koshelev, A. I. Larkin. and V. M. Vinokur. Phys. Rev. B **50**, 16770 (1994).

[34] L. Burlachkov, Phys. Rev. B **47**, 8056 (1993).

[35] G. Blatter, M. V. Feigel'man, V. B. Geshkenbein, A. I. Larkin. and V. M. Vinokur, Rev. Mod. Phys. **66**, 1125 (1994).

[36] Y. M. Wang, A. Zettl, S. Ooi, and T. Tamegai, Phys. Rev. B **65**, 184506 (2002).

[37] S. Ooi, T. Shibauchi, and T. Tamegai, Physica C **302**, 339 (1998).

[38] A. Yurgens, M. Konczykowski, N. Mros, D. Winkler, and T. Claeson, Phys. Rev. B **60**, 12480 (1999).

[39] T. Tamegai et al., Physica C **341C-348C**, 1507 (2000).

[40] T. Tamegai, Y. Iye, I. Oguro, and K. Kishio, Physica C **213**, 33 (1993).

[41] T. Giamarchi and P. L. Doussal, Phys. Rev. B **55**, 6577 (1997).

[42] Y. Kopeievich and P. Esquinazi, J. Low Temp. Phys. **1**, 113 (1998).

[43] R. Wördenweber and P. H. Kes, Phys. Rev. B **34**, 494 (1986).

[44] R. S. Berry, Nature **393**, 212 (1998).

[45] A. N. Goldstein, C. M. Echer, and A. P. Alivisatos, Science **256**, 1425 (1992).

[46] M. F. Goffman et al., Phys. Rev. B **57**, 3663 (1998).

[47] D. Ertas and D. R. Nelson, Physica C **272**, 79 (1996).

[48] J. Kierfeld and V. Vinokur, Phys. Rev. B **61**, 14928 (2000).

[49] M. J. P. Gingras and D. A. Huse, Phys. Rev. B **53**, 15193 (1996).

[50] A. I. Larkin and Y. N. Ovchinnikov, J. Low Temp. Phys. **34**, 409 (1979).

[51] T. Schuster et al., Phys. Rev. Lett. **73**, 1424 (1994).

[52] E. H. Brandt, Phys. Rev. B **60**, 11939 (1999).

[53] A. V. Kuznetsov, D. V. Eremenko, and V. N. Trofimov, Phys. Rev. B **56**, 9064 (1997).

[54] Y. M. Wang, A. Zettl, S. Ooi, and T. Tamegai, Physica C **341C-348C**, 3626 (2000).

[55] S. Berry, M. Konczykowski, P. H. Kes, and E. Zeldov, Physica C **282-287**, 2259 (1997).

[56] M. Nideröst et al., Phys. Rev. Lett. **81**, 3231 (1998).

[57] E. Zeldov et al.. EuroPhys. Lett. **30**, 367 (1995).

[58] E. H. Brandt, Phys. Rev. B **59**, 3369 (1999).

[59] N. Morozov, E. Zeldov, M. Konczykowski, and R. Doyle. Physica C **291**, 113 (1997).

[60] J. Chiaverini, K. Yasumura, and A. Kapitulnik. Phys. Rev. B **64**. 014516 (2001).

[61] A. E. Koshelev, Phys. Rev. Lett. **83**, 187 (1999).

[62] S. Nakaharai, T. Ishiguro. S. Watauchi, J. Shimoyama. and K. Kishio, Physica C **357-360**, 552 (2001).

[63] M. S. Fuhrer. K. Ino, K. Oka, Y. Nishihara, and A. Zettl. Solid State Commun **101**. 841 (1997).

[64] L. Bulaevskii, M. Maley, H. Safar, and D. Domnguez. Phys. Rev. B **53**. 6634 (1996).

[65] K. Kadowaki and T. Mochiku, Physica B **194-196**, 2239 (1994).

[66] S. Aukkaravittayapun. P. King, Y. Latyshev, and R. Bowley. Physica C **277**. 196 (1997).

[67] A. E. Koshelev, Phys. Rev. Lett. **76**, 1340 (1996).

[68] L. Bulaevskii. M. Ledvij, and V. Kogan, Phys. Rev. B **46**. 366 (1992).

[69] M. F. Crommie, G. Briceño, , and A. Zettl, Phys. Rev. B **45**, 13148 (1992).

[70] Y. Paltiel et al., Phys. Rev. Lett. **85**, 3712 (2000).

[71] A. Mazilu et al.. Phys. Rev. B **58**, 8913 (1998).

[72] S. F. W. R. Rycroft et al., Phys. Rev. B **60**, 757 (1999).

[73] J. Mirkovic, S. E. Savel'ev. E. Sugahara, and K. Kadowaki, Phys. Rev. Lett. **86**. 886 (2001).

[74] D. López, E. F. Righi, G. Nieva, and F. de la Cruz, Phys. Rev. Lett. **76**, 4034 (1996).

[75] C. D. Keener. M. L. Trawick, S. M. Ammirata, S. E. Hebboul, and J. C. Garland. Phys. Rev. Lett. **78**, 1118 (1997).

[76] D. T. Fuchs et al.. Phys. Rev. B **55**. 6156 (1997).

[77] T. T. M. Palstra, B. Batlogg, R. B. van Dover, L. F. Schneemeyer. and J. V. Waszczak. Phys. Rev. B **41**, 6612 (1990).

[78] X. G. Qiu, V. V. Moshchalkov, and J. Karpinski, Phys. Rev. B **62**. 4119 (2000).

[79] T. Blasius et al.. Phys. Rev. Lett. **82**. 4926 (1999).

[80] S. Ijima, Nature **354**, 56 (1991).

[81] C. N. R. Rao. R. Sen, B. Satishkumar, and J. Govindaraj, J. Chem. Soc.. Chem. Commun. **15**. 1525 (1998).

[82] N. S. Hamada. S. Sawada. and A. Oshiyama, Phys. Rev. Lett. **68**. 1579 (1992).

[83] T. W. Odom, H. Jin-Lin, P. Kim, and C. M. Lieber, Nature **391**. 62 (1998).

[84] M. S. Dresselhaus, G. Dresselhaus, and P. C. Eklund. *Science of Fullerenes and Carbon Nanotubes*, Academic Press, San Diego, CA, 1996.

[85] S. J. Tans, A. R. M. Verschueren, and C. Dekker, Nature **393**, 49 (1998).

[86] M. M. J. Treacy, W. Ebbesen, and J. M. Gibson, Nature **381**, 678 (1996).

[87] T. Rueckes et al., Science **289**, 94 (2001).

[88] C. Zhou, J. Kong, E. Yenilmez, and H. Dai, Science **290**, 1552 (2000).

[89] P. G. Collins, K. Bradley, M. Ishigami, and A. Zettl, Science **287**, 1801 (2000).

[90] J. Kong et al., Science **287**, 622 (2000).

[91] J. Kong, H. T. Soh, A. M. Cassell, C. F. Quate, and H. Dai, Nature **395**, 878 (1998).

[92] Y. Zhang et al., Appl. Phys. Lett. **79**, 3115 (2001).

[93] K. Yamamoto, S. Akita, and Y. Nakayama, Jpn. J. Appl. Phys. Part2 **35**, L917 (1996).

[94] K. Yamamoto, S. Akita, and Y. Nakayama, J. Phys. D **31**, L34 (1998).

[95] X. Q. Chen, T. Saito, H. Yamada, and K. Matsushige, Appl. Phys. Lett. **78**, 3714 (2001).

[96] J. Liu et al., Chem. Phys. Lett. **303**, 125 (1999).

[97] J. C. Lewenstein, T. P. Burgin, A. Ribayrol, L. A. Nagahara, and R. K. Tsui, Nano. Lett. **2**, 443 (2002).

[98] B. H. Fishbine, Full. Science and Tech. **4**, 87 (1996).

[99] M. Ahlskog, R. Tarkiainen, L. Roschier, and P. Hakonen, Appl. Phys. Lett. **77**, 4037 (2000).

[100] P. G. Collins, M. S. Arnold, and P. Avouris, Science **292**, 706 (2001).

Appendix A

Fabrication of GaAs/AlGaAs Hall Sensor

Since we use GaAs/AlGaAs Hall sensors in local magnetization measurements of BSCCO, we describe here the Hall sensor fabrication techniques. GaAs/AlGaAs wafers are supplied by Prof. Tamegai at University of Tokyo, Japan. Local Hall sensors are fabricated from those GaAs/AlGaAs wafers using the facilities here at the Microfabrication Laboratory (MicroLab) at UC Berkeley. Figure A shows a whole Hall sensor device containing an array of six Hall sensors. Since GaAs is a fragile (and expensive) material that can be easily damaged, cautions should be taken when handling GaAs chips. I describe below the Hall sensor fabrication procedure starting with a 15mm×15mm GaAs chip.

(a) Cut a small scratch on one side of the chip using a scriber. Put the scriber underneath the scratch and then push down on both side of the chip with two fingers. The chip breaks easily.
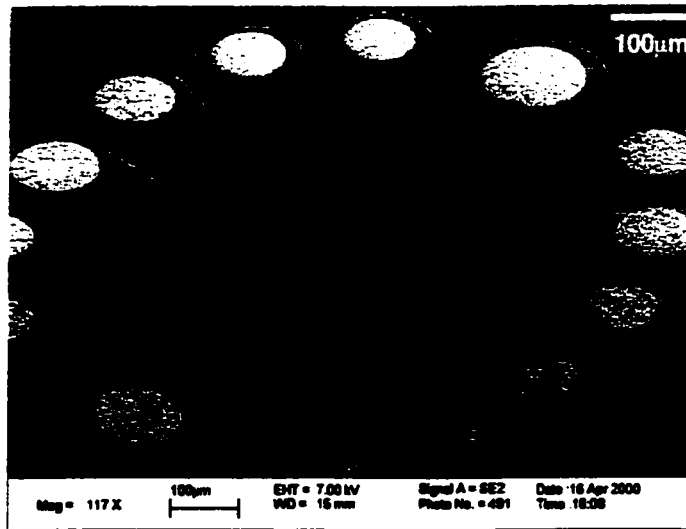
Figure A.1: Array of six Hall sensors.

(b) Obtain 5 × 5 mm² chips. Since photoresist does not adhere to GaAs surfaces well, the chips are first placed in a DCE bubble bath for 5 min to help in its adhesion of photoresist in the next step.

(c) Spin on photoresist (Shipley 1818) at 6000 rpm, anneal at 90°C for 6 min. and then expose and develop the Hall sensor structure.

(d) With the photoresist covering the Hall sensor area as a mask, the chip is dipped into a $H_2SO_4:H_2O:H_2O_2$ mixture to etch away the unwanted areas. This etching step is to isolate the 2D electron gas layer between the GaAs and the AlGaAs layers. The 1:8:80 ratio mixture is made by adding water first, sulfuric acid second, and H_2O_2 last. The mixture should be stirred well before etching. The etch rate of GaAs is ≈0.5 μm/min.

(e) After etching, rinse the chip in de-ionized water.

(f) Pattern and develop contact pads on top of the etched Hall sensor.

(g) Evaporate germanium (500 Å) and then gold (1000 Å) without breaking the vacuum.

(h) Lift off the photoresist to reveal the Hall sensor with contacts.

(i) Since germanium forms Schottky barriers at GaAs interfaces, the contacts are annealed in "forming gas" (10% H_2 and 90% N_2) at 380°C for 30 sec to reduce the contact resistance from the original $M\Omega$ range.

(j) "Wire-bond" the contacts using the techniques described in Appendix B. Ordinary wire-bonding should not be used here because of the fragile GaAs surface.

Appendix B

Wire-bonding of Micron-sized

Contacts

We normally use three methods to connect wires to a sample. In one method, silver paint (or silver epoxy) is used as glue and gold wires are connected to samples by hand. This method requires a contact that is at least 200×200 μm^2 in size. For contact areas in the range of 100 μm wide, wire-bonding methods may be used on hard materials. For delicate single crystals like BSCCO, the wiring-bonding method will damage the sample surface. When contact areas smaller than 100 μm are required, as with the micron-sized Corbino disk contacts on a BSCCO single crystal (Fig. B.1), the wire-bonding method is also insufficient. We have developed a new technique to connect gold wires to micron-sized contacts without damaging the sample surface. This method uses a commercial wire-bonder to connect gold wires of one or one half of a mil wide ($\approx$ 30 μm) onto sample surfaces using silver paint as glue. Here we describe this wire-bonding method. The manipulators of
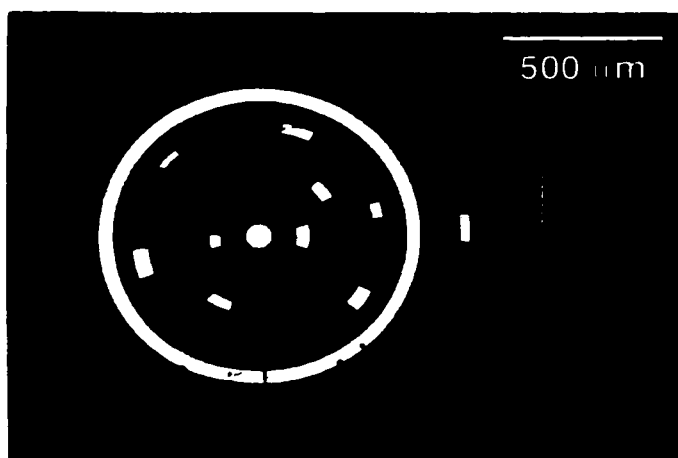
Figure B.1: Corbino disk contacts on a BSCCO single crystal.

typical wire-bonders are very stable. This enables us to connect gold wires to patterned contact pads with high precision.

a. One mil gold wires are cut into 1 cm long pieces. Place one wire in the clamp of the wire-bonder (Westbond 7600 in MicroLab).

b. Mix a small puddle of silver paint with thinner (EB Acetate) on a small chip. The viscosity level should be medium. Thinner or thicker mixtures are both harder to stick onto gold wires.

c. The silver paint mixer is placed next to the sample on the bonder under the microscope. Bend the tip of the gold wire slightly, then use the manipulator of the wire-bonder to dip the wire's tip into the silver paint. When a small silver paint ball forms at the tip, quickly bring it to the contact pad on the sample and lower the handle to connect.

d. Stay still for approximately 40 second allowing the silver paint to dry. Open the clamp, leaving the gold wire standing on the contact. Release the handle.
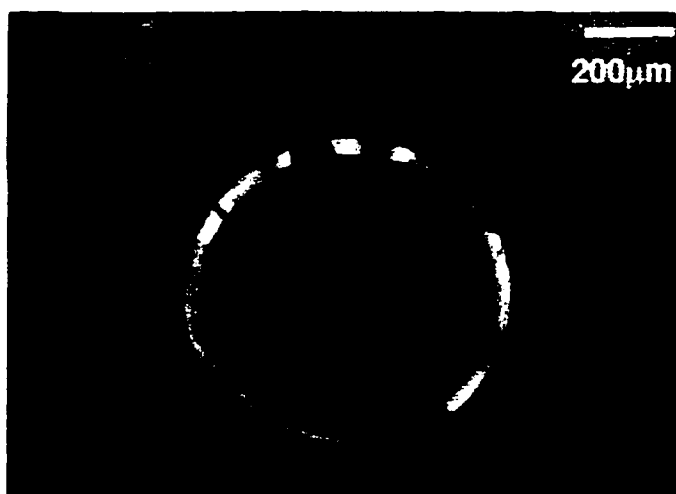
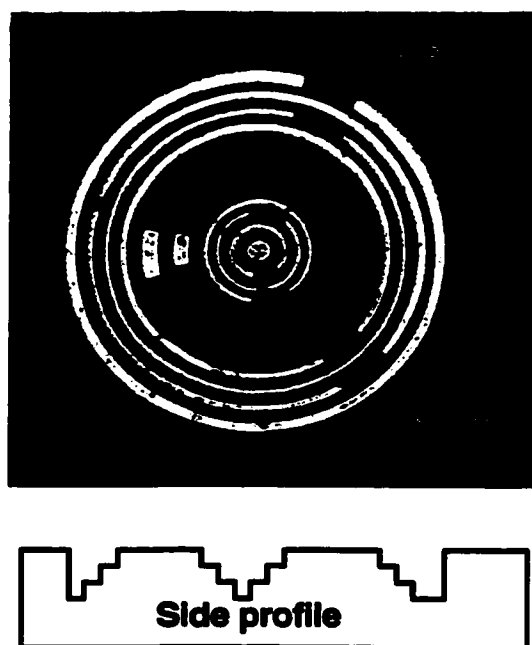Figure B.2: Wiring of micron-sized Corbino disk contacts.

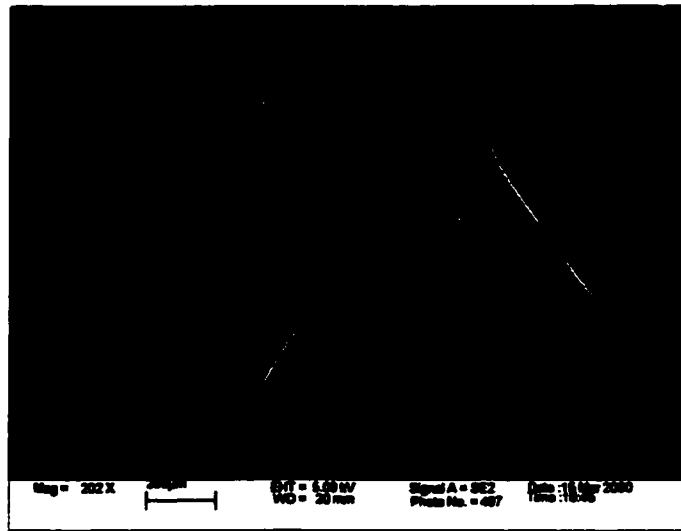Figure B.3: Another Corbino disk pattern where disks are etched into the sample at different depths.

Figure B.4: An SEM image of the wiring Corbino disk contacts.

e. The silver paint mixture dries quickly and becomes too thick for good deposition in a few minutes. It should be changed once every two or three depositions.

A bonded Corbino disk sample using this method is shown in Fig. B.2. Notice the silver paint contacts are roughly the same size as the original contact pads underneath. Figure B.3 shows a different Corbino disk pattern, where the disks are etched down into the sample as shown in the side profile. This design is to study the c-axis correlated vortex behavior where currents are sent from all depths. Figure B.4 is an SEM image showing the wiring of this sample. Darker photoresists are seen around all contacts acting as protective insulating-layers to keep over-spilled silver paint from touching neighboring contacts.